Imperial College London (UK)
Department of Chemical Engineering

Modelling framework for a low-grade heat thermofluidic oscillator: The Evaporative Reciprocating Piston Engine

Internship report
Period: 30 June 2014 - 31 October 2014

Author:
M.A.G. Timmer
Student number: s1008153
m.timmer-1@student.utwente.nl

Supervisors:
Dr. Christos Markides (ICL)
Prof. Dr. Ir. Theo van der Meer (UT)

On behalf of:
University of Twente
Faculty of Engineering Technology (CTW)
Thermal Engineering department

Preface

This report describes the work of my four month internship period at the Chemical Engineering Department of Imperial College London. This internship is part of the Master curriculum of Mechanical Engineering at the University of Twente.

First of all, I would like to thank Dr. Christos Markides and Prof. Dr. Ir. Theo van der Meer for making my internship possible. I would like to thank Theo for the great opportunities he presented me with, after stating him my personal preferences for my internship. I would like to thank Christos for his guidance throughout my project and the great and fruitful discussions we have had about a range of different subject. I can honestly say that I have learned a lot during my four month period at Imperial College, much more than I had imagined I would.

I would especially like to thank Aly Taleb, who has helped me a lot to understand the difficult subjects we have worked with. He was always available when I had a problem or question, and took all the time needed to help me therewith. Next to Aly, I would really like to thank Christoph Kirmse, who has really helped me get going in the beginning of my internship, by answering all my questions and introducing me to everyone in the group. I also really enjoyed setting up and performing the experiments together. I would like to thank the rest of the group as well, for making me feel very welcome, whether it was during meetings, lunch time or non-work related events they invited me for.

I would also like to thank my girlfriend Franka Koehoorn, who has really supported me (as always) during my work, and had decided to come to London with me and experience all the great things here together. Next to that, I would like to thank my family and friends for their moral support, and keeping me in the loop of their personal lives during my stay in London.

Thanks to you all, it has been a true pleasure.

Michael Timmer
London, Friday 31 October 2014

Abstract

This work presents the construction of a modelling framework for the Evaporative Reciprocating Piston Engine (ERPE). This engine belongs to the group of thermofluidic oscillators, in which steady boundary conditions cause oscillatory, thermodynamic behaviour by evaporation and condensation of a working fluid. Due to the constant temperature phase change, these engines are able to operate across small temperature differences between the heat source and heat sink, thus they are able to utilize low-grade heat and convert it into power.

The modelling framework for describing the ERPE makes use of the electrical analogy between the fluid and thermal domain with the electrical domain. In this analogy, voltage represents a pressure/temperature difference and a current represents a volumetric/entropy flowrate. The engine is divided into independent, linearised and spatially lumped components, for which the governing equations are represented in the electrical domain. This results in an electrical circuit representation of the ERPE, where the passive electrical components of the circuit are resistors, inductors and capacitors. For the heat exchanger of the engine, two linear models are investigated. The first model imposes a linear temperature profile along the heat exchanger wall (the LTP model) and the second model imposes a linear power input gradient along the heat exchanger wall and the dynamic ability to store and release energy (the DHX model).

For validation purposes, both models are solved to acquire their performance indicators, such as operating frequency and exergy efficiency, which are then compared with experimental results from an early stage ERPE prototype. These comparisons show that the LTP model is not able to capture the correct behaviour of the ERPE prototype, especially in the cases were the load component of the prototype was set to high resistances. The DHX model was able to predict the behaviour of the ERPE prototype up to the correct order of magnitude, especially for the cases were the load was set to high resistances, which are the most realistic cases to represent the actual engine with. It can therefore be concluded that the DHX model can be used for predicting the behaviour of the ERPE correctly within an order of magnitude, whilst the LTP model can not.

The DHX model was then used to perform a parametric study, which gave insight into the trends in the performance indicators with changing operating conditions or design variables of the engine. These results can subsequently be used to optimize future designs of the ERPE, which should eventually lead to a full-scale design of an ERPE for power production using low-grade heat. For the latter purpose, it is suggested to not only use the linear model of the current work, but also develop a nonlinear model. This model would be able to better describe the nonlinear behaviour that certain components of the engine exhibit, and therewith predict the behaviour of the entire ERPE more accurately.

As a prequel for a nonlinear model, experiments have been done to identify the temperature profile along the heat exchanger wall, which is needed to develop a nonlinear model. These experiments showed that the temperature profile of the heat exchanger wall can be described with a tanh function. The analysis of 18 sets of experimental data, with changing operating conditions for every experiment, showed that the slope of the tanh function at the zero point is almost constant for all cases. Therefore, the nonlinear model can use a tanh function, with the identified slope from the experiments, as a temperature profile for the heat exchanger wall.

Contents

List of Figures

List of Tables

Nomenclature

A . . . . Area (m^2)

C . . . . Electrical capacitance equivalent (kg^{-1} m^4 s^2)

D . . . . Diameter (m)

E . . . . Electrical voltage equivalent (kg m^{-1} s^{-2})

I . . . . Electrical current equivalent (m^3 s^{-1})

L . . . . Electrical inductance equivalent (kg m^{-4})

P . . . . Absolute pressure (kg m^{-1} s^{-2})

R . . . . Radius (m)

R . . . . Electrical resistance equivalent (kg m^{-4} s^{-1})

T . . . . Temperature (K)

U . . . . Volumetric flowrate (m^3 s^{-1})

V . . . . Volume (m^3)

Z . . . . Electrical impedance equivalent (kg m^{-4} s^{-1})

Υ . . . . Constant related to the load model (-)

$\dot{S}$ . . . . Entropy flow (J K^{-1} s^{-1})

η . . . . Efficiency (-)

γ . . . . Heat capacity ratio (-)

λ_1 . . . . Constant related to the load model (-)

λ_2 . . . . Constant related to the load model (-)

μ . . . . Viscosity (kg m^{-1} s^{-1})

ω . . . . Angular frequency (rad s^{-1})

ρ . . . . Density (kg m^{-3})

c_p . . . . Specific heat capacity (J kg^{-1} K^{-1})

g . . . . Gravitational acceleration (m s^{-2})

h . . . . Convective heat transfer coefficient (kg K^{-1} s^{-3})

h . . . . Height (m)

k . . . . Feedback gain (-)

l . . . . Length (m)

m . . . . Mass (kg)

s . . . . Specific entropy (J kg^{-1} K^{-1})

1 Introduction

This chapter provides the introduction to the performed work, and is sectioned as follows. First, the background and motivation are given in section 1.1. Subsequently, the description of the researched engine design is given in section 1.2. Finally, the research goals and the outline of this report are given in section 1.3.

1.1 Background and motivation

On a global average, by far the largest proportion of power is generated by using fossil fuels such as coal, natural gas and oil. The combustion of fossil fuels leads to the emission of so called green house gases. It's becoming a widely known fact that these green house gases have a detrimental effect on our global climate, and therewith, the environment and living conditions for all life across the globe. Next to these harmful emissions the resources of oil, natural gas and coal are approximated to be depleted in 35, 37 and 107 years, respectively [1]. These problems can be partly tackled by increasing the efficiency of the current fossil fuel technologies, but mainly by alternative means of power generation.

Great progress has been made with renewable energy sources, i.e., energy sources that are continuously restored such as solar energy and wind energy. Despite that, still progress has to be made to improve the technology and market position of renewable energy source technologies, such that it can replace, or at least take over a large proportion of, the power generation of fossil fuels.

A group of energy sources that overlaps with renewable energy sources is low-grade heat. Low-grade heat can be heat from either renewable energy sources, such as solar energy or geothermal energy, or waste heat from industrial processes. In the latter case, the utilization of waste heat can be regarded as increasing the overall efficiency of a current process, rather than a different energy source. Therefore, low-grade heat covers both the increase of efficiency of current fossil fuel technologies and the alternative means of power generation. Next to that, the abundance of low-grade heat [2] and its low environmental impact makes the utilization of low-grade heat an economically viable and competitive solution for the fossil fuel problems mentioned in the first paragraph.

There is no clear agreement on the definition of low-grade heat. For example, it could be defined as any heat available below 250°C as in [3], or as heat that can not be recovered within a certain process as in [2]. However, for the purpose of this report it is sufficient to think of low-grade heat as heat that is too low in comparison with the environment to be utilized in conventional power generating devices. This immediately raises the question of which devices are able to operate across such a small temperature difference.

Thermofluidic oscillators are one such class of devices which use steady thermal boundary conditions to induce thermodynamic (e.g. pressure and temperature), heat and fluid oscillations [4]. Examples of thermofluidic oscillators include liquid-piston Fluidyne engines [5] and gas-cycle thermoacoustic engines [6, 7]. One particularly interesting type of thermofluidic oscillators for low-grade heat is the kind where a working fluid is evaporated at the hot heat exchanger and condensed at the cold heat exchanger. The phase change of the working fluid occurs at a constant temperature, and therefore the temperature gradient between the heat source and sink of the engine can be small, as is the case when using low-grade heat.

An inherent consequence of the small temperature difference between the heat source and sink is a low Carnot efficiency [8], when compared to the high energy counterparts of fossil fuel technologies. This means that in practice the thermal efficiency of low-grade heat technologies will never reach the thermal efficiency of fossil fuel technologies. However, due to the abundance of low-grade heat [2] its costs are really low when compared with fossil fuels, which prices will continue to increase due to the depletion of these energy sources. This, combined with the increased reliability due to the lack of mechanically moving parts in thermofluidic oscillators, results in the advantages of lower operating and maintenance costs [9].

An example of such a two-phase thermofluidic oscillator, with the properties given above, was presented by Smith [4, 10, 11] as the Non-Inertive-Feedback Thermofluidic Engine (NIFTE). The working principle of the engine examined in this work is closely related to that the NIFTE, but the design is quite different. The main difference is that there is a mechanical piston, instead of a liquid piston as in the NIFTE. Next to that, the compartments and interconnections that contain the working fluid are configured in a different way. This new design is referred to as the Evaporative Reciprocating Piston Engine (ERPE), and its design and working principle will be explained in the next section.

1.2 Evaporative Reciprocating Piston Engine

1.2.1 Design

The Evaporative Reciprocating Piston Engine (ERPE) design is based on an early-stage prototype at the Boreskov Institute of Catalysis (BIC) at Novisibirsk, Russia [12]. The main parts of the ERPE are the displacer cylinder, working cylinder and the connection tube, as can be seen from the schematic in figure 1.

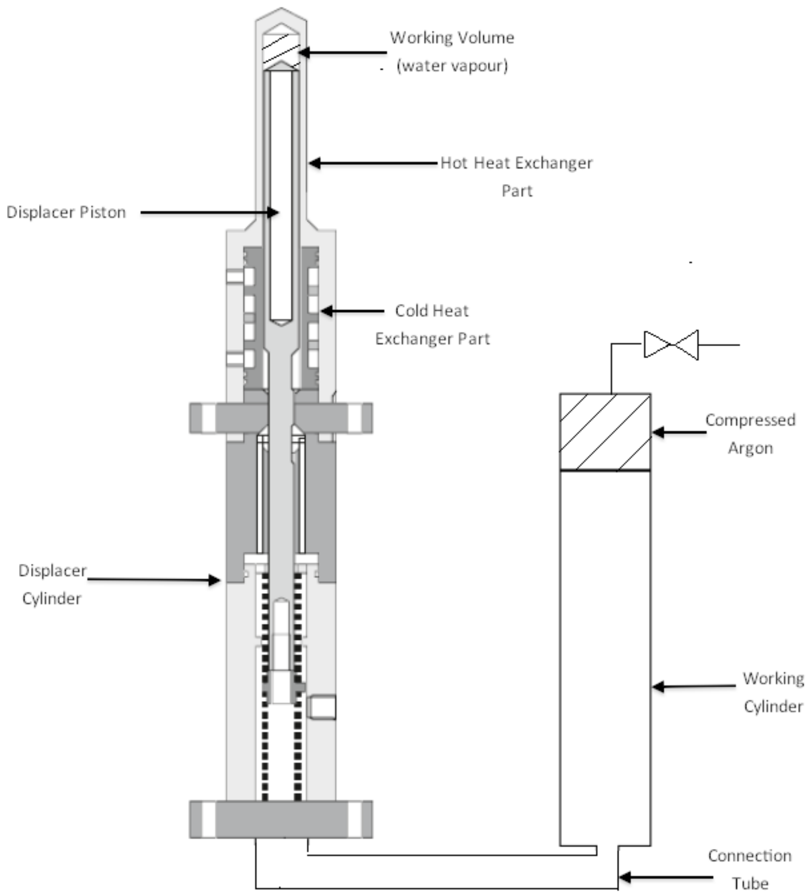

Figure 1: Schematic of the ERPE prototype

The displacer cylinder, shown in the left part of the schematic, houses the hot heat exchanger and the cold heat exchanger. In the prototype the hot heat exchanger is a catalytic heater, which causes the working fluid (in this case water) to evaporate, but this could be any type of heat exchanger depending on the form of low-grade heat. The cold heat exchanger uses cooling water to subtract heat from the working fluid and causes condensation of it. The displacer piston, which is a mechanical piston, has a specific shape such that it also acts as a valve (see figure 2). When the valve is closed the working fluid on top of the piston, in the so called working volume, is sealed from the working fluid below the displacer piston. Depending on the vertical position of the displacer piston, the valve is either closed or opened. The final component in the displacer cylinder is a mechanical spring, depicted by the black blocks beneath the displacer piston.

The working cylinder, shown in the right part of the schematic, houses liquid working fluid beneath a section of compressed argon of constant mass. The time-mean pressure of the argon, called the back-pressure, can be set by the valve shown on top of the working cylinder. Displacement of the working fluid in the working cylinder causes expansion or compression of the argon, which subsequently acts as a 'gas spring'.

The connection tube, shown in the bottom of the schematic, connects the displacer cylinder and the working cylinder and is completely filled with working fluid. The total volume of liquid at the bottom of the displacer cylinder, inside the connection tube and at the bottom of the working cylinder serves as a liquid piston that transmits volumetric changes from the working volume to the gas spring [12]. The connection tube also contains an adjustable check valve, where the pressure drop across the valve serves as a load, and is thus used to measure the work output generated by the ERPE. In later works of the ERPE the valve will be replaced with an actual load, such as a hydraulic load, which will deliver actual power output.

1.2.2 Working principle

During operation the ERPE undergoes repeating cycles. To understand the working principle, it is therefore sufficient to understand one operating cycle. For this description, it is assumed that the cycle starts at the equilibrium position, as shown in figure 1. At this stage the valve is closed, as shown in the middle schematic of figure 2. The hot heat exchanger adds heat to the working fluid in the working volume, thus evaporating the working fluid. This increases the pressure above the displacer piston, and because the pressure beneath the displacer piston stays nearly constant, a pressure difference across the piston is established. This pressure difference forces the piston downwards, thus compressing the mechanical spring and the gas spring; where the latter is compressed by the movement of the working fluid through the connection tube. In the connection tube the work is also utilized in the load, albeit only when the piston is moving in a downward direction.

When the piston has moved near the bottom dead center the valve opens, as shown in the right schematic of figure 2, and the pressure above and beneath the piston suddenly equalizes. At this stage the working fluid in the compartment above the valve reaches the cold heat exchanger, which causes the working fluid to undergo condensation. Simultaneously the downward motion of the piston is slowed down and finally reversed to an upward motion, due to the influence of the compressed mechanical spring and gas spring. This closes the valve again, whilst the condensation of the working fluid continues. A pressure difference is again established across the piston, but due to the condensation the pressure difference now forces the piston in the upward direction.

When the piston has travelled upwards near the top dead center, the valve opens again, as shown in the left schematic of figure 2. This causes the pressure above and below the piston to be equalized again. At that stage the working fluid has begun evaporating under the influence of the hot heat exchanger, whilst the mechanical spring and gas spring force the piston direction to reverse. This closes the valve again and a pressure difference across the piston is established due to the evaporation of the working fluid. The pressure difference, along with the mechanical spring and gas spring, force the piston in a downward motion to the equilibrium position, which closes the description of one operating cycle.

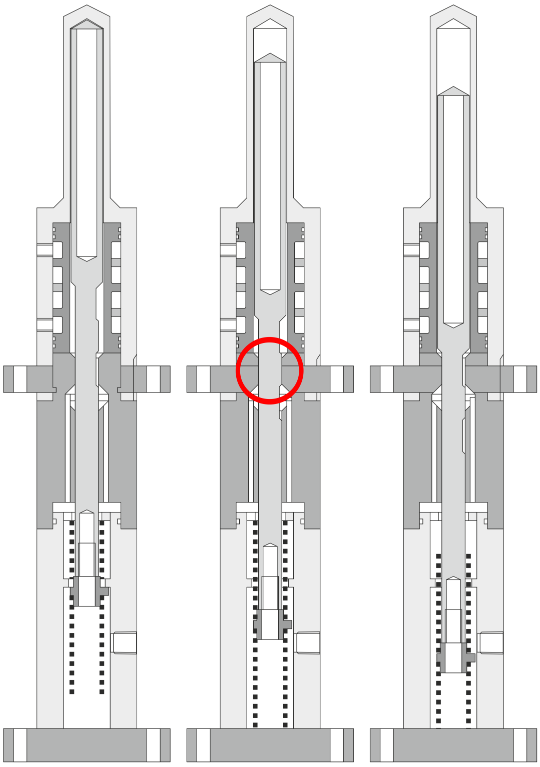

Figure 2: Schematic of the position of the displacer piston with the corresponding valve state. The valve is open when the displacer piston is at or near the top dead centre (left) or bottom dead center (right), and is closed otherwise (middle).

Now that the working principle of the ERPE is clear, it is worth noting a few advantages of this two-phase Stirling engine when comparing it with conventional ones [12]:

- This engine is more cost efficient relative to gas-phase Stirling engines, due to the reduced heat transfer area required associated with higher heat transfer coefficients that can be reached during the phase change process.
- The engine has a more effective sealing of the working fluid.
- The engine does not require lubrication for surfaces that incorporate friction, since the working fluid in its liquid state can act as a lubricant.
- The working fluid existing in the liquid phase in parts of the engine reduces the dead volume.

1.3 Research goals and outline

The main goal of this research work is to develop a model that can predict the behaviour of the ERPE. This model can be validated by the use of experimental results, which were acquired using the early-stage prototype in Russia. Once validated, the model can be used to determine an optimal design from a parametric study. Note that an optimal design means optimal performance indicators, such as the exergetic efficiency and oscillation frequency of the modelled engine.

The modelling framework of the Non-Inertive Feedback Thermofluidic Engine (NIFTE) showed that its modelling method was able to predict the behaviour of experimental results of a prototype. Because of the analogy between the NIFTE and the ERPE, this modelling framework therefore seems a good starting point for the current model. This framework should be adjusted and extended, where needed, to optimize the predicting behaviour of the ERPE model.

Next to the main part of this work, as described above, some work will be done on determining the temperature profile along the displacer cylinder wall. This temperature profile can be used as an input for a future non-linear model of the ERPE. For this purpose an experimental set-up has been designed. During this work the experimental set-up should be constructed and the experiments should be performed. By analysing the results of the experiments, a way of setting the non-linear temperature profile along the cylinder wall should be given.

To acquire the aforementioned goals, a certain methodology will be used, which will be described in chapter 2. After that, the model validation and parametric study will be presented in chapter 3. This chapter will present the results of the modelling framework and it will analyse and discuss the results. The experimental part, including a description of the set-up, will then be given in chapter 4. Finally, the main conclusions and drawbacks of this work will be given in chapter 5.

2 Methodology

As mentioned in the introduction of this report, the used methodology for modelling the ERPE is similar to that of the NIFTE. This report will mainly describe the work done to adjust and extend this modelling framework for the application with the ERPE. However, to make this report comprehensible, details about the basics of the modelling will also be provided. For full detail of the complete modelling framework the reader is referred to the first work done by Smith [10, 11, 4, 13], and the later extension of that work by Solanki [14, 15, 16].

2.1 Electrical analogy

The modelling approach of the ERPE is based on the analogy between specific components of the engine and electric components. The engine is sectioned into different regions were distinct heat transfer or fluid flow processes take place. This region is then linearized, such that a combination of spatially lumped linear components forms the description of the entire engine. The electrical analogy between the spatially lumped linear components and passive electrical components, such as resistors, inductors and capacitors, ensures that the physical engine can be described by an analogous electrical (RLC) circuit. Note that this approach captures the first order effects in the physical system, but does not represent the non-linear dynamics of the system [17].

For the description of the ERPE, electrical analogies will be drawn with resistors, inductors and capacitors, were:

- Resistors are used to describe heat transfer and viscous drag
- Inductors represent fluid inertia
- Capacitors represent hydrostatic pressure and vapour compressibility

As mentioned before, analogies will be drawn either in the fluid domain or the thermal domain, depending on the dominant process in that region. In the fluid domain, a pressure (P) difference across a physical component is analogous to a voltage (E) difference across an equivalent electrical component. Next to that, the volumetric flowrate (U) through the same physical component is analogous to the current (I) through the equivalent electrical component. In the thermal domain, a temperature (T) difference across a physical component is analogous to a voltage drop (E) across the equivalent electrical component, whilst the entropy flow ($\dot{S}$) is analogous to the current (I) through the equivalent electrical component.

To complete the electrical analogy, the description of a resistor, inductor and capacitor need to be given in terms of their electrical parameters. The description of a resistor is given by Ohm's law as,

$$E = RI \tag{2.1}$$

where R is the resistance of the resistor. The description of an inductor is given by Faraday's law of induction as,

$$E = L\frac{dI}{dt} \Longrightarrow E = sLI \tag{2.2}$$

where L is the inductance of the inductor and the right hand side expression is the equivalent of the left hand side expression in the Laplace domain. Finally, the description of a capacitor is derived from Gauss's law as,

$$\frac{dE}{dt} = \frac{I}{C} \Longrightarrow E = \frac{1}{sC}I \tag{2.3}$$

where C is the capacitance of the capacitor and the right hand side expression is the equivalent of the left hand side expression in the Laplace domain.

2.2 Model development

As briefly mentioned before, the ERPE in sectioned into different parts; each with its own dominant behaviour in either the fluid domain or the thermal domain. For this purpose, the ERPE has been divided into different subsections, as can be seen from figure 3. For each subsection the governing equations are derived, which will be used to determine the analogous electrical components to be placed in an electrical (RLC) circuit. Note that this approach looks at the thermal domain and fluid domain independently, and afterwords couples both domains together with the relations given in section 2.2.2.

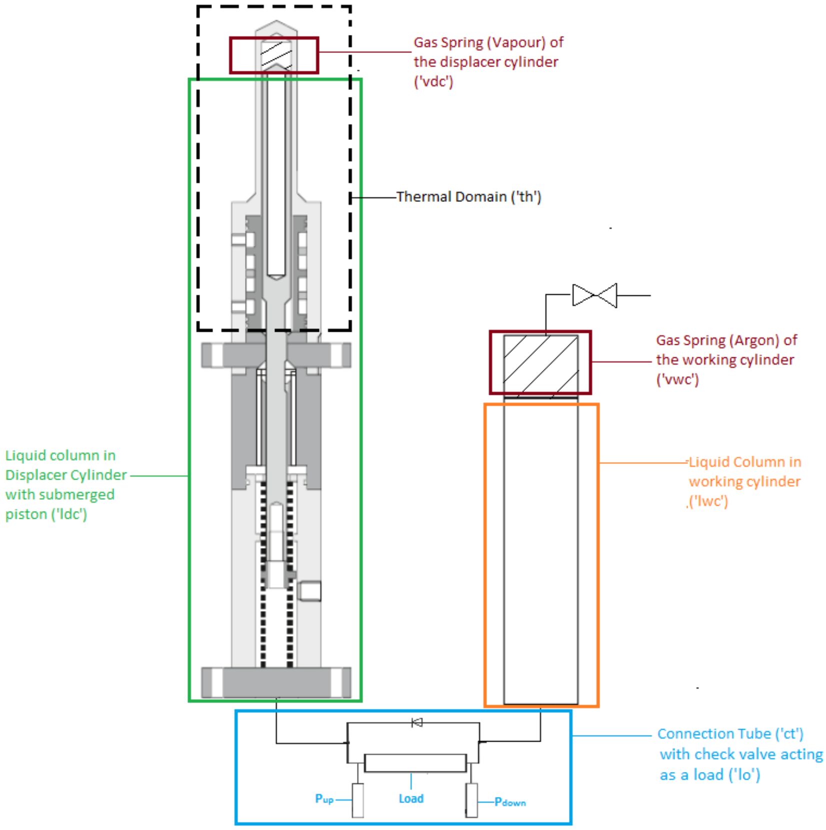

Figure 3: Schematic of the ERPE prototype, where the different subsections indicate distinct heat transfer or fluid flow processes

When deriving the governing equations for the different subsections, it is useful to note that the ERPE is a periodic, oscillation device. This enables one to express the thermodynamic quantities as a decomposition of time-mean values and a fluctuating component, where the time average of the fluctuating component is zero by definition. As an example, the time-mean flowrate is denoted by $\overline{U}$, and its fluctuating component by U' (so $\overline{U'} = 0$). Following Solanki et al. [16], a number of simplifications and conventions are now given to simplify the governing equations:

- Since the ERPE is a purely oscillating (zero-mean) flow device, only the fluctuating components around their respective time-means are taken into account.
- It is assumed that all time-varying quantities exhibit only small perturbations around their respective time means, e.g. $U' \ll \overline{U}$.
- For simplicity, because only the fluctuating components are considered, the primes are dropped from the notation, e.g. $U'(t) \to U(t)$.

2.2.1 Fluid domain

This section will provide the derivation of the governing fluid domain equation and the electrical analogy for the gas spring in the working cylinder (denoted by subscript 'v,wc'). This should give one insight into how the governing physical equations are transformed into their electrical analogies. For clearance of this report, the full derivations of the other subsections are not given, but they can be found in the aforementioned NIFTE papers. The results for all subsections, as a function of resistances, inductances and capacitances, are given in table 1 in section 2.2.3.

The gas spring in the working cylinder is periodically compressed and expanded. It is assumed that the compression and expansion of the gas is isentropic, i.e. adiabatic and reversible. It can then be shown that the pressure-volume relation is given by,

$$P_{v,wc}(V_{v,wc})^{\gamma} = constant \tag{2.4}$$

were $P_{v,wc}$ and $V_{v,wc}$ are the time-varying pressure and volume of the gas spring, respectively, and γ is the heat capacity ratio of the working fluid (argon in this case). The time derivative of the pressure-volume relation yields,

$$\frac{1}{P_{v,wc}}\frac{dP_{v,wc}}{dt} + \frac{\gamma}{V_{v,wc}}\frac{dV_{v,wc}}{dt} = 0 \tag{2.5}$$

The pressure and volume can be expressed as the sum of the time-averaged mean and the fluctuation around this mean, i.e. $P_{v,wc} = P_0 + P'_{v,wc}$ and $V_{v,wc} = V_{0,v,wc} + V'_{v,wc}$. Note that P_0 is the equilibrium pressure, or back-pressure, of the engine. Using that the time derivatives of P_0 and $V_{0,v,wc}$ are zero and assuming small oscillations around the time-averaged mean (e.g. $V'_{v,wc} \ll V_{0,v,wc}$),

$$\frac{1}{P_0}\frac{dP'_{v,wc}}{dt} + \frac{\gamma}{V_{0,v,wc}}\frac{dV'_{v,wc}}{dt} = 0 \tag{2.6}$$

The derivative of $V'_{v,wc}$ with respect to time is equal to minus the net volumetric flowrate into and out of the vapour volume, i.e. $\frac{dV'_{v,wc}}{dt} = -U_{v,wc}$. Finally, dropping the primes, as stated as a convention in the previous section,

$$\frac{dP_{v,wc}}{dt} = \frac{\gamma P_0}{V_{0,v,wc}}U_{v,wc} \tag{2.7}$$

Equation 2.7 can now be compared with the characteristic equation for a capacitor (equation 2.3) in the Laplace domain,

$$\frac{dP_{v,wc}}{dt} = \frac{\gamma P_0}{V_{0,v,wc}}U_{v,wc} \Longrightarrow sP_{v,wc} = \frac{\gamma P_0}{V_{0,v,wc}}U_{v,wc} = \frac{1}{C_{v,wc}}U_{v,wc} \tag{2.8}$$

where $C_{v,wc}$ is the corresponding capacitance of the gas spring in the working cylinder, which is given by,

$$C_{v,wc} = \frac{V_{0,v,wc}}{\gamma P_0} \tag{2.9}$$

Note that this result, along with the results for the other subsections, can also be found in table 1 in section 2.2.3.

2.2.2 Thermal domain

The heat exchanger is one of the most difficult components to model; especially due to the complexity of the two-phase heat transfer process. In this section, two methods to model the heat exchanger will be given. The first model assumes a linear temperature profile (LTP) along the heat exchanger wall, whilst the second assumes a linear power input along the heat exchanger wall. The latter also accounts for the storage of energy in the solid heat exchanger walls, and is thus called a dynamic heat exchanger (DHX). Before presenting these two heat exchanger models, the coupling between the fluid domain and the thermal domain is given first.

Coupling the fluid and thermal domain

In section 2.1 the analogy between the fluid domain and the thermal domain with the electrical domain was given. It stated that the temperature and pressure were analogous to the voltage, and that the volumetric flowrate and entropy flow were analogous to the current. To complete this description, the coupling between the pressure and temperature and the coupling between the volumetric flowrate and entropy flow are needed. The latter follows from the large change in density that takes place during the phase change, and is given by,

$$\dot{S}_{th} \approx \rho_{g,0} \Delta s_{fg} U_{th} \tag{2.10}$$

were $\rho_{g,0}$ is the time-averaged density of the working fluid in the vapour phase and $\Delta \mathrm{s}_{fg}$ is the change in entropy due to the evaporation.

The coupling between the temperature and pressure can be derived from the Clausis-Clapeyron relation. It is assumed that the phase change processes only exhibit small perturbations around the time-mean saturation temperature T_0 and pressure P_0. The coupling between the temperature and pressure is then given by,

$$T_i = \left(\frac{dT}{dP}\right)_{sat} P_i \tag{2.11}$$

were $(dT/dP)_{sat}$ is the change in temperature with respect to pressure along the saturation curve around the mean point.

Linear temperature profile (LTP) model

The LTP model assumes a linear temperature profile along the heat exchanger wall, as depicted on the left hand side of figure 4. It is assumed that the heat transfer from the heat exchanger to the working fluid is governed by convection, and that all heat transport is purely associated with the phase change process. The relation of the heat exchanger in the thermal domain is then given by,

$$\dot{S}_{th} = \frac{\dot{Q}}{T_0} = \frac{hA_s}{T_0}(T_{hx} - T_{ad}) \tag{2.12}$$

where T_{hx} is the temperature of the heat exchanger as a function of height, T_{ad} is the temperature of the working fluid, T_0 is the time-averaged saturation temperature of the fluid, h is the convective heat transfer coefficient and A_s is the area of the heat exchanger taking part in the phase change process. The time-averaged saturation temperature of the working fluid is assumed to equal the mean temperature of the heat exchanger, i.e. $T_0 \equiv \overline{T}_{ad} = \overline{T}_{hx}$. Equation 2.12 can now be converted into the fluid domain by using the coupling equations 2.10 and 2.11 to give,

$$P_{th} - P_{ad} = \frac{\rho_{g,0} T_0 \Delta s_{fg}}{hA_s \left(\frac{dT}{dP}\right)_{sat}} U_{th} = R_{th} U_{th} \tag{2.13}$$

where R_{th} represents the thermal resistance. When equation 2.13 is compared to the characteristic equation of a resistor (equation 2.1), it is clear that the thermal resistance is given by,

$$R_{th} = \frac{\rho_{g,0} T_0 \Delta s_{fg}}{hA_s \left(\frac{dT}{dP}\right)_{sat}} \tag{2.14}$$

Note that this equation is also listed in table 1 in section 2.2.3.

The derivation given above results in the electrical analogy of a resistor for the heat exchanger, but is doesn't set the linear temperature profile along it. This will be done in section

2.2.3, by setting the feedback gain of the electrical (RLC) circuit presented in that section.

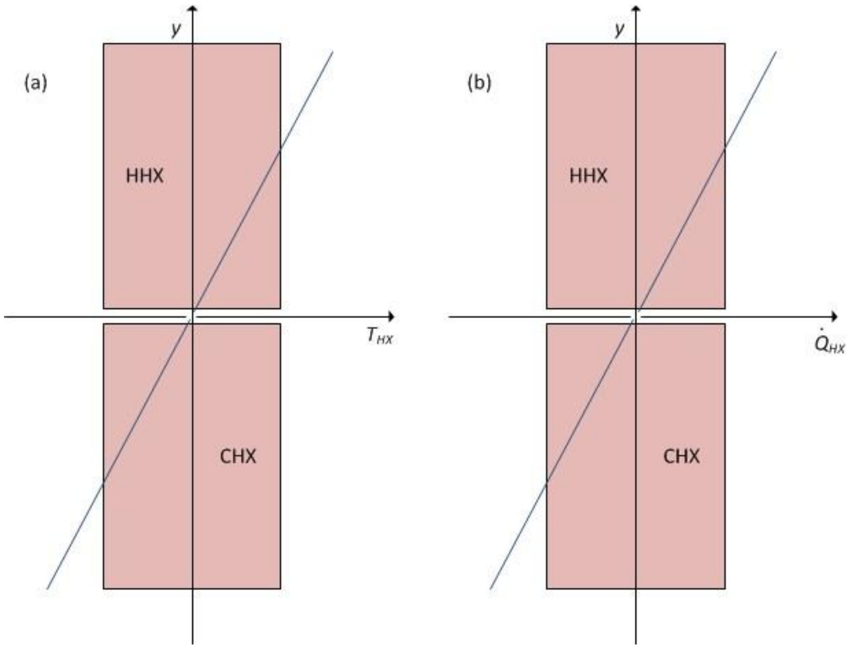

Figure 4: The linear temperature profile of the LTP model (left) and the linear power gradient of the DHX model (right)

Dynamic heat exchanger (DHX) model

The DHX model differs from the LTP model in that it assumes a linear power input along the heat exchanger instead of a linear temperature profile, as can be seen from the right hand side of figure 4. Next to that, the DHX model accounts for the ability the store and release energy in the solid heat exchanger wall as the working fluid evaporates and condenses [14]. When including this capacity of the heat exchanger wall, the governing equation in the thermal domain is given by,

$$\dot{Q}_{hx} - mc_p\left(\frac{dT_{hx}}{dt}\right) = hA_s(T_{hx} - T_{eq}) \tag{2.15}$$

where $\dot{Q}_{hx}$ is the heat addition and subtraction at the outside of the heat exchanger wall, m is the mass of the heat exchanger wall that takes place in the heat transfer process and c_p is the heat capacity of the heat exchanger wall. Note that in the DHX model the temperature of the heat exchanger wall, T_{hx}, is a function of time.

Equation 2.15 can now be converted into the fluid domain by substituting the coupling equations 2.10 and 2.11 to give,

$$U_{th} = \frac{mc_p(dT/dP)_{sat}}{\rho_{g,0}T_0\Delta s_{fg}}\left(\frac{dP_{hx}}{dt}\right) + \frac{hA_s(dT/dP)_{sat}}{\rho_{g,0}T_o\Delta s_g}(P_{th} - P_{ad}) \tag{2.16}$$

Equation 2.16 can be compared to the characteristic equation of a capacitor (2.3) plus a resistor (2.1), which is of the following form,

$$U_{th} = C_{hx}\frac{dP_{hx}}{dt} + \frac{1}{R_{th}}(P_{th} - P_{ad}) \tag{2.17}$$

where C_{hx} is the capacitance of the heat exchanger wall. It is clear that the thermal resistance R_{th} is the same as the thermal resistance of the LTP model. Next to that, there is a capacitance term describing the capacitance of the heat exchanger wall, which is given by,

$$C_{hx} = \frac{mc_p(dT/dP)_{sat}}{\rho_{g,0}T_0\Delta s_{fg}} \tag{2.18}$$

Note that this equation is also listed in table 1 in section 2.2.3.

The derivation given above results in the electrical analogy of a resistor and a capacitor for the heat exchanger, but is doesn't set the linear power input along it. This will be done in section 2.2.3, by setting the feedback gain of the electrical (RLC) circuit presented in that section.

2.2.3 Electrical (RLC) circuit

In the previous sections the electrical analogy and the coupling between the fluid domain and thermal domain were given. Next to that, some examples of deriving the electrical analogy for specific engine components were given. Analogous to these derivations, the complete ERPE can be described in terms of resistances, inductances and capacitances. The results of these derivations are given in table 1.

Table 1: Expressions of the electrical parameters for all subsections

Parameter	Description/Effect	Expression
	Working Cylinder flow resistance (drag)	$R_{l,wc} = 128\mu_w l_{lwc}/\pi D_{wc}^4$
	Connection tube flow resistance (drag)	$R_{\mathrm{ct}} = 128\mu_w l_{ct}/\pi D_{ct}^4$
	Piston flow resistance	$R_{\mathrm{p}} = 4h_{\mathrm{p}}\mu/\pi R_{\mathrm{p}}^2 C_1$
	Leakage flow resistance (wall interface)	$R_{l1} = 8C_2 h_{\mathrm{p}}\mu/\pi C_1 C_4$
Resistance (R_i)	Leakage flow resistance (piston interface)	$R_{l2} = -8C_2 h_{\mathrm{p}}\mu/\pi C_1\left(2C_2 R_{\mathrm{p}}^2 + C_1\right)$
	Piston Resistance at slide bearing section	$R_{\mathrm{sb,p}} = 2\mu_w l_{channel}/\pi {R_{\mathrm{sb,p}}}^3\delta$
	Leakage resistance in slide bearing	$R_{\mathrm{sb,l}} = 128\mu_w l_{channel}/\pi {D_{channel}}^4$
	Displacer cylinder flow resistance (drag)	$R_{l,dc} = 128\mu_w(l_c + l_a)/\pi {D_{dc}}^4$
	Thermal Resistance	$R_{th} = \rho_{\mathrm{g,0}}T_0\Delta s_{\mathrm{fg}}/hA_{\mathrm{s}}(\mathrm{d}T/\mathrm{d}P)_{\mathrm{sat}}$
	Working cylinder hydrostatic capacitance	$C_{\mathrm{l,wc}} = \mathrm{A}_{wc}/\rho_w g$
	Vapour compressibility (working cylinder)	$C_{\mathrm{v,wc}} = V_{\mathrm{0,wc}}/P_0\gamma_{\mathrm{argon}}$
	Vapour compressibility (displacer cylinder)	$C_{\mathrm{v,dc}} = V_{\mathrm{0,vdc}}/P_0\gamma_{\mathrm{w}}$
Capacitance (C_i)	Displacer cylinder hydrostatic capacitance	$C_{\mathrm{l,dc}} = \mathrm{A}_{dc}/\rho_w g$
	Piston capacitance due to spring	$C_{\mathrm{p}} = -\pi R_{\mathrm{p}}^2 C_1/2kC_2$
	Leakage capacitance	$C_l = \pi^2 C_1\left(2C_2R_{\mathrm{p}}^2 + C_1\right)/4C_2^2 k$
	Heat storage capacitance	$C_{hx} = mc_p(dT/dP)_{sat}/\rho_{g,0}T_0\Delta s_{fg}$
	Working cylinder inertia	$L_{\mathrm{l,wc}} = \rho_w l_{lwc}/A_{wc}$
	Connection tube inertia	$L_{\mathrm{ct}} = \rho_w l_{ct}/A_{ct}$
	Piston inertia	$L_{\mathrm{p}} = -2m_p C_2/\pi^2 R_{\mathrm{p}}^2 C_1$
	Leakage inertia	$L_{\mathrm{l}} = 4C_2^2 m_{\mathrm{p}/\pi^2 C_1(2C_2R_{\mathrm{p}}^2+C_1)}$
	Piston inertia at slide bearing section	$L_{\mathrm{sb,p}} = \mu_{wl_{channel}}/\pi {R_{\mathrm{sb,p}}}^2$
Inductance (L_i)	Leakage inertia in slide bearing	$L_{\mathrm{sb,l}} = \mu_{wl_{channel}}/A_{channel}$
	Displacer cylinder inertia	$L_{l,dc} = \rho_w\big[l_c\big(2/A_{dc} - Z_{p,l,total}/A_p Z_{p,total} - Z_{p,l,total}/A_l Z_{l,total}\big) + l_a\big(Z_{p,l,total}/A_p Z_{p,total} + Z_{p,l,total}/A_l Z_{l,total} - 1/A_{dc}\big)\big]$

The values of the resistances, inductances and capacitances can be seen as design variables for the engine. Next to that, some of the variables change with different operating conditions, such as the back-pressure. Using the design of the prototype of the ERPE in Russia, the nominal values for the parameters given in table 1 are estimated. The nominal values of the parameters that do not change with changing operating conditions are given in table A1 in appendix A. The nominal values of the parameters that do change with changing back-pressure are given in table A2 in appendix A. The latter are given for the six different back-pressures that were used to acquire experimental results, such that the model can be validated with the experimental results, as will be attempted in chapter 3.

Now that the electrical analogies for all the engine components are known, the electrical components are placed in an electrical (RLC) circuit. This electrical circuit for the LTP model is depicted in figure 5(a) and the electrical circuit for the DHX model is depicted in figure 5(b). To clarify these figures and the large amount of parameters, the same subsections as for the physical engine in figure 3 are given in figure 5(a). The different boxes in the electrical circuit thus represent the different subsections of the physical engine. It should finally be noted that both the LTP model and the DHX model do not include a load for power generation. This load, as shown in the connection tube of figure 3, will be derived in section 2.2.4 and subsequently electrical circuits for the load case will be given. This division is made because three experiments have been performed without a load, and three experiments have been performed with a load. By constructing both the no-load and load-case models it is ensured that all experimental data can be used for the validation of the model.

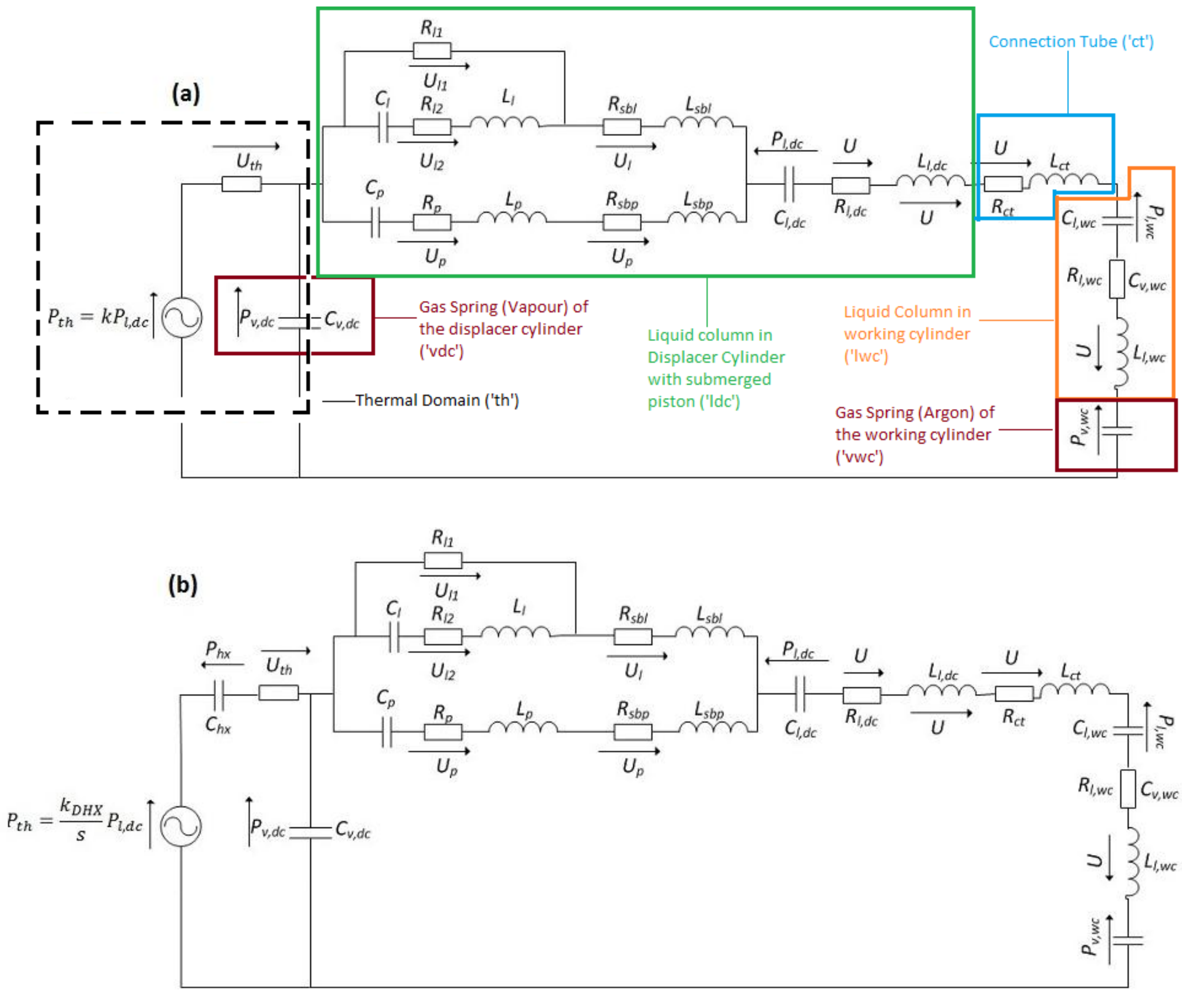

Figure 5: The electrical (RLC) circuit for the no-load case of (a) The LTP model and (b) The DHX model.

As mentioned in the section 2.2.2, the linear temperature profile for the LTP model and the linear power input for the DHX model will be set by the feedback gain k. In both models, the feedback gain is defined as: $k = P_{th}/P_{l,dc}$, were $P_{l,dc}$ is the hydrostatic pressure of the working fluid on top of the piston. It is important to realize that this hydrostatic pressure is proportional to the height of the working fluid along the heat exchanger wall.

The relation for the feedback gain of the LTP model is found by using the Clausis-Clapeyron relation (equation 2.11) for P_{th} and the definition of the hydrostatic pressure above the piston for $P_{l,dc}$, i.e. $P_{l,dc} = \rho_w g y$, were y is the height of the working fluid. The relation for the feedback gain is then given by,

$$k = \frac{P_{th}}{P_{l,dc}} = \frac{T_{hx}(y)}{\rho_w g y \left(\frac{dT}{dP}\right)_{sat}} \tag{2.19}$$

For the LTP model, the temperature gradient along the heat exchanger wall is linear, i.e.,

$$\frac{T_{hx}(y)}{y} = \frac{dT_{hx}}{dy} \tag{2.20}$$

Therefore, the feedback gain is given by,

$$k = \frac{dT_{hx}/dy}{\rho_w g \left(\frac{dT}{dP}\right)_{sat}} \tag{2.21}$$

From equation 2.21 it is clear that, since the denominator is constant for a given set-up, the feedback gain is linearly proportional to the temperature gradient along the heat exchanger wall. In section 2.3, the procedure of finding a solution for the LTP model will be given, which will include finding the feedback gain at marginal stability. In a physical sense, this is thus equivalent to finding a temperature gradient along the heat exchanger wall which is just sufficient for steady, non-decaying oscillations in the engine.

The relation for the feedback gain of the DHX model is still found by using the definition of the hydrostatic pressure for $P_{l,dc}$. However, the relation for P_{th} is found by using Norton's theorem or the equivalent Thévenin's theorem. These theorems can be used to describe the relation between voltage sources and current sources, such that the voltage source P_{th} can be described in terms of the current source U_{th} (and therewith $\dot{Q}_{hx}$). For Alternating Current (AC) circuits these theorems couple the voltage source and current source through an impedance Z, which in this case is given by: $Z = 1/(sC_{hx})$. The coupling therefore becomes,

$$P_{th} = \frac{U_{th}}{sC_{hx}} \tag{2.22}$$

Using that $U_{th} = \dot{Q}_{hx}/(\rho_{g,0} T_0 \Delta s_{fg})$, the relation for the feedback gain is given by,

$$k = \frac{P_{th}}{P_{l,dc}} = \frac{1}{s} \frac{\dot{Q}_{hx}}{\rho_w g y \rho_{g,0} T_0 \Delta s_{fg} C_{hx}} \tag{2.23}$$

For the DHX model, the power input gradient along the heat exchanger wall is linear, i.e.,

$$\frac{\dot{Q}_{hx}}{y} = \frac{d\dot{Q}_{hx}}{dy} \tag{2.24}$$

Therefore, the feedback gain is given by,

$$k = \frac{k_{DHX}}{s} = \frac{1}{s} \frac{d\dot{Q}_{hx}/dy}{\rho_w g \rho_{g,0} T_0 \Delta s_{fg} C_{hx}} \tag{2.25}$$

were k_{DHX} is the constant part of the feedback gain. It is clear from equation 2.25 that the feedback gain is linearly proportional to the power input gradient along the heat exchanger, for a specific s.

Due to the linearisation assumptions above, the solution of the model will be purely sinusoidal, and therefore the Laplace variable $s = i\omega$, were ω is the angular frequency. The factor s can thus be physically explained by the fact that the storage of energy in the heat exchanger wall depends on the oscillation frequency of the engine. The feedback constant is thus not only dependent on the gradient along the heat exchanger wall, as in the LTP model, but it is also dependent on the oscillation frequency.

2.2.4 Load model

In this section the method to model the load will be given. The load model requires special attention because its modelling is significantly different from other components and other load models, which were done in the same electrical analogy framework. The load section, which will be modelled in accordance with the ERPE prototype, consists of an adjustable check valve, two pressure sensors and another check valve. These components can be seen in the connection tube of figure 3. The actual load is the adjustable check valve, which will only work during half of the operating cycle because of the double check valve set-up.

Pressure measurements upstream ('P_{up}') and downstream ('P_{down}') of the adjustable check valve ('Load'), as shown in figure 3, have been performed for three valve settings. They indicate that this valve cannot be accurately represented by a simple resistance, as has been done in previous studies [13, 14, 15, 16]. Figure 6 plots the ratio of the amplitudes of the experimental pressures downstream and upstream of the valve $|P_{\text{down}}/P_{\text{up}}|$ in the frequency domain, which are acquired using an FFT algorithm. A single resistance would return an approximately constant amplitude ratio for all frequencies. As can be seen from figure 6, this is unrealistic around the operating frequency at which the valve measurements have been done.

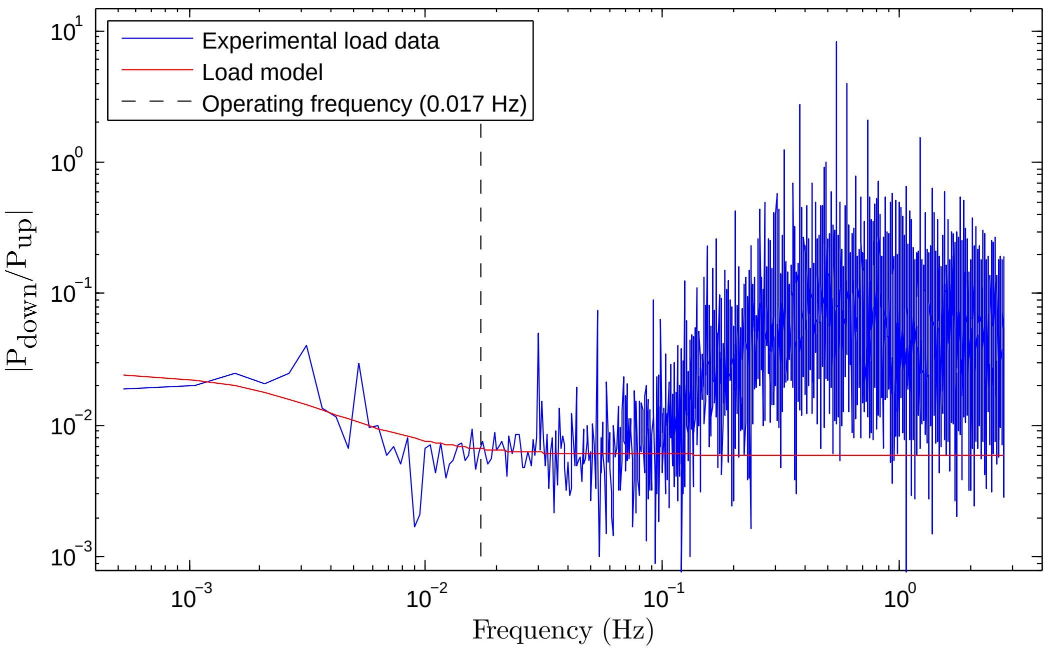

Figure 6: In blue: plot of the amplitude ratio $|P_{down}/P_{up}|$ of the experimental data with the valve set to the highest steady flow resistance and 5 bar back-pressure. In Red: plot of the fitted load model according to equation 2.30. In Black: a dotted line which shows the frequency at which the ERPE prototype was oscillating with the according valve setting and back-pressure.

For at least one order of magnitude above and below the operating frequency, the spectral data follows the trend of the following relation, which is represented by the red graph in figure 6.

$$\frac{P_{\text{down}}}{P_{\text{up}}} = \Upsilon \frac{1 + s\lambda_1}{1 + s\lambda_2} \tag{2.26}$$

where $s = i\omega$ is the Laplace variable and Υ, λ_1 and λ_2 are constants that depend on the valve setting. For each valve setting, Υ, λ_1 and λ_2 are fitted such that the relation follows the spectral distribution as closely as possible, especially in the vicinity of the operating frequency. The results of these fittings for the other two valve settings are depicted in figures B1 and B2 in appendix B.

The dimensionless relation of equation 2.26 provides the pressure drop across the valve as a function of s, but it does not provide the impedance which relates the pressure drop and volumetric flowrate across it, i.e. $\Delta P = ZU$. As in the case of simple resistors, inductors and capacitors, this relation is needed to represent the model in the electrical analogy framework. The relation is found by using experimental pressure drop and flowrate measurements for steady flow, which is equivalent to $s = 0$ (no oscillation). For each valve setting multiple pressure and flowrate measurements have been performed, of which the averaged values yield the steady flow resistance as follows,

$$R_{\text{exp}} = \frac{P_{\text{up}} - P_{\text{down}}}{U} \tag{2.27}$$

where R_{exp} is the steady flow resistance and U is the volumetric flowrate. It is assumed that R_{exp} is constant for every operating frequency, and thus that the change of the load with varying frequency is purely described by equation 2.26. The complete load model can then be found by combining the pressure drop as a function of s (equation 2.26), with the relation between the pressure drop and the volumetric flowrate (equation 2.27). For this purpose equation 2.26 is rewritten to the form,

$$(P_{\text{up}} - P_{\text{down}}) \left[\frac{1 + s\lambda_2}{\Upsilon(1 + s\lambda_1)} \right] = \frac{P_{\text{up}}}{\Upsilon} \left[\frac{1 + s\lambda_2}{1 + s\lambda_1} - \Upsilon \right] = UR_0 \tag{2.28}$$

The expression on the left hand side in the square brackets is dimensionless, therefore equation 2.28 is similar to $\Delta P = ZU$, so the final equation sets the relation between the pressure drop and the volumetric flowrate just as in equation 2.27. R_0 is a yet to be determined constant with the same unit as R_{exp}. Evaluating equation 2.28 for the case of $s \to 0$ and equating to the experimental measurements of equation 2.27 shows that,

$$R_0 = \frac{R_{\text{exp}}}{\Upsilon} \tag{2.29}$$

Equation 2.28, with the help of equation 2.29, can be rewritten as

$$\frac{P_{\text{up}} - P_{\text{down}}}{Z_{\text{lo},1}} = \frac{P_{\text{up}} - 0}{Z_{\text{lo},1} + Z_{\text{lo},2}} = U \tag{2.30}$$

where $Z_{\text{lo},1}$ and $Z_{\text{lo},2}$ are the impedances describing the load and the relation between the state downstream of the load and the ground respectively,

$$Z_{\text{lo},1} = \Upsilon R_0 \frac{1 + s\lambda_1}{1 + s\lambda_2} \quad Z_{\text{lo},2} = \Upsilon^2 R_0 \frac{(1 + s\lambda_1)^2}{(1 + s\lambda_2 - \Upsilon(1 + s\lambda_1))(1 + s\lambda_2)} \tag{2.31}$$

Note that $P_{\text{up}} - 0$ is the pressure drop across load valve *and* the whole working cylinder. Therefore, $Z_{\text{lo},1} + Z_{\text{lo},2}$ accounts for the components (resistors, inductors and capacitors) of the load and of everything downstream of the pressure sensor 'P_{down}' in figure 3 (mainly the working cylinder). To make sure the working cylinder components aren't modelled twice, they thus have to be removed from the electrical circuit for the load models, because they are already modelled in the impedances of the load model.

The implementation of the load model of equation 2.30 in the electrical circuit is done by placing the two impedances in series, as is depicted in figure 7(a) for the LTP model and in figure 7(b) for the DHX model.

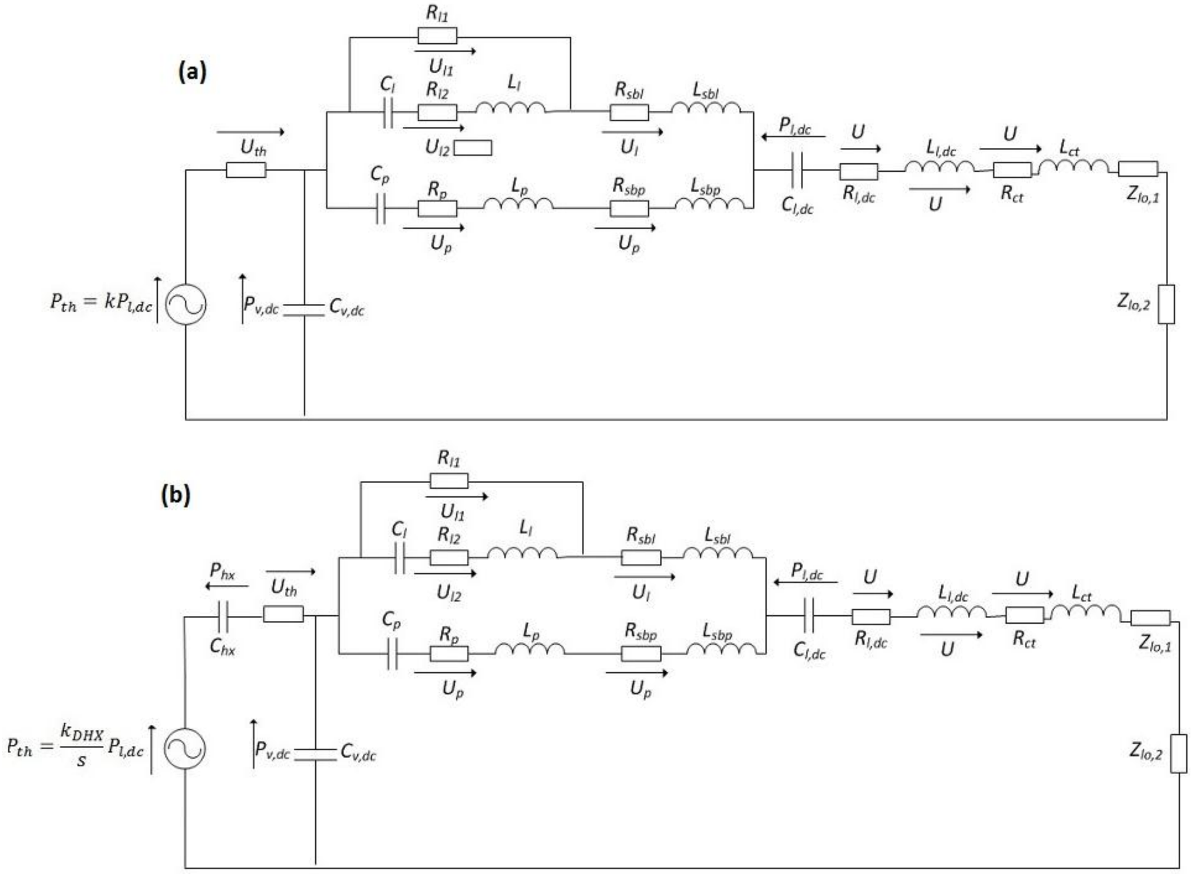

Figure 7: The electrical (RLC) circuit for the load case of (a) The LTP model and (b) The DHX model.

2.3 Solving the model

In this section the method to solve the electrical model will be explained. What exactly is meant by solving the model will become clear further on in this section. At first it is needed to define some transfer functions and give the expression of these transfer functions in terms of the components shown in the electrical (RLC) circuits. For this purpose, it is convenient to write each component, or group of components, as an impedance with an according subscript. For example, the impedance of the connection tube, which consists of a resistance and an inductance, is denoted by $Z_{ct} = R_{ct} + sL_{ct}$.

The definition of the forward-loop transfer function $G(s)$ is given by:

$$G(s) = \frac{P_{l,dc}}{P_{th}} = \frac{P_{l,dc}}{P_{v,dc}} \frac{P_{v,dc}}{P_{th}} \tag{2.32}$$

were the right hand side consists of the transfer functions $\alpha = P_{v,dc}/P_{th}$ and $\beta = P_{l,dc}/P_{v,dc}$. The terms α and β can be found by applying Kirchoff's current and voltage laws for the electrical circuits. Note that there is a distinction between the no-load models and load models, as shown in figures 5 and 7, respectively, and that there is a distinction between the LTP (a) and DHX (b) models. The results for α and β for all four models can be found in table 2.

Table 2: Transfer function for the LTP and DHX models

	$\alpha = P_{v,dc}/P_{th}$	$\beta = P_{l,dc}/P_{v,dc}$
LTP (no load)	$1 - R_{th}/Z_{tot,LTP}$	$(1/(\alpha Z_{tot,LTP}) - sC_{v,dc})(Z_a + Z_p) - 1$
LTP (load)	$1 - R_{th}/Z_{tot,lo,LTP}$	$(1/(\alpha Z_{tot,lo,LTP}) - sC_{v,dc})(Z_{lo} + Z'_a + Z_p) - 1$
DHX (no load)	$1 - (R_{th} + 1/s/C_{hx})/Z_{tot,DHX}$	$(1/(\alpha Z_{tot,DHX}) - sC_{v,dc})(Z_a + Z_p) - 1$
DHX (load)	$1 - (R_{th} + 1/s/C_{hx})/Z_{tot,lo,DHX}$	$(1/(\alpha Z_{tot,lo,DHX}) - sC_{v,dc})(Z_{lo} + Z'_a + Z_p) - 1$

In table 2 several impedances appear. These impedances are groupings of components and are found by simple electrical addition laws for parallel and serial circuits. For example Z_a, which is a grouping of the impedances of the liquid in the displacer cylinder, the connection tube and the working cylinder for the no-load case, is given by:

$$Z_a = Z_{wc} + Z_{ct} + Z_{l,dc} = 1/s/(C_{l,wc} + C_{v,wc}) + R_{l,wc} + sL_{l,wc} + R_{ct} + sL_{ct} + 1/s/C_{l,dc} + R_{l,dc} + L_{l,dc} \tag{2.33}$$

The other impedances that appear are, Z_p, which is the total impedance of the piston and leakage part, Z_{lo}, which is the impedance of the load model ($Z_{\mathrm{lo},1}$ + $Z_{\mathrm{lo},2}$) and Z_{tot}, which is the total impedance of the electrical circuit. Working out these impedances from the electrical circuit, just as was done for Z_a, then yields the forward-loop transfer function $G(s) = \alpha\beta$ for the four different models.

Using the forward-loop transfer function, the closed-loop transfer function $C(s) = P_{l,dc}/P_{th}$ can be found, were $P_{l,dc}$ and P_{th} are now the closed loop states. The representation of the closed-loop is depicted in figure 8. Examining this circuit yields,

$$(P_{th} + k_i P_{l,dc})G(s) = P_{l,dc} \tag{2.34}$$

so,

$$P_{th}G(s) = P_{l,dc}(1 - k_i G(s)) \tag{2.35}$$

Rearranging shows that the closed-loop transfer function is given by,

$$C(s) = \frac{P_{l,dc}}{P_{th}} = \frac{G(s)}{1 - k_i G(s)} \tag{2.36}$$

were k_i is the feedback gain, which was defined for the LTP and DHX model is section 2.2.3).

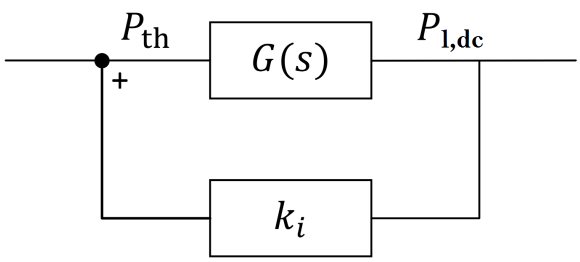

Figure 8: Closed-loop representation of the ERPE, where $G(s)$ is the forward-loop transfer function and k_i is the feedback gain.

To find the behaviour of the closed-loop system, for a given set of (RLC) parameters and a feedback gain, one should look at the closed-loop poles. The closed-loop poles are the values of

s for which the denominator of the closed-loop transfer function becomes zero. The poles are of the form: $s = \sigma \pm i\omega$, and appear as purely real ($\omega = 0$) are as complex conjugate pairs. There are three possible outcomes for the behaviour of the system in a linear model: stable, unstable and marginally stable. Stable behaviour arises when all poles have a negative real part, i.e. $\sigma < 0$, which causes all oscillations to decay exponentially. Unstable behaviour arises when at least one pole has a positive real part, i.e. $\sigma > 0$, in which the oscillations with a positive real part pole grow exponentially. Finally, marginally stable behaviour is acquired when one pair of complex conjugate poles is purely imaginary, i.e. $\sigma = 0$, and all other poles have negative real parts. In the latter case one oscillation is sustained, i.e. it doesn't grow or decay, and all other oscillations decay exponentially.

The marginal stability of the system is the point at which the ERPE is assumed to be operating. Thus, for a given set of (RLC) parameters, a feedback gain should be found which causes one pair of complex conjugate poles to become completely imaginary, whilst the other poles all have negative real parts. In a physical sense, finding this gain is equivalent to finding what the temperature gradient or power input gradient, for respectively the LTP model and the DHX model, should be.

Initially, in the NIFTE work, the required gain was found by using the SISOTOOL of MATLAB, were the poles were manually moved up to the point were one pole reached the imaginary axes. In this work, the method of finding the feedback gain is replaced by an iterative method. It starts at a very low value of the feedback gain and then increases it by big steps. At every step the closed-loop poles are examined, and the process is continued until one pole crosses the imaginary axis. At that point that feedback gain is set back to the previous step and the magnitude of the increase per step is reduced significantly. After a few iterations, this will yield the value of the feedback gain up to the desired accuracy, and therewith the feedback gain to reach marginal stability of the system. At this value of the feedback gain the performance of the system is examined using some performance indicators, which will be presented in the next section.

2.4 Performance indicators

To validate the performance of the model, the results of the model can be compared to the experimental results acquired from the ERPE prototype. For this purpose some performance indicators, upon which the performance of the model is examined, should be defined. The performance indicators should be possible to acquire from the model as well as from the experimental results, to ensure a comparison is possible. A problem hereof is that the linear model only yields ratio's between the state variables of the system, but not the actual values of e.g. pressures and temperatures itself. On the other hand, the experimental results don't provide enough information the acquire the ratio of two state variables, they only provide the specific variables at one point as a function of time. This results in the fact that the amplitudes of the pressure and temperature cannot be validated with the experimental results. One advantage of a future non-linear model would be that these amplitudes can be used as a performance indicator of the model.

One very important performance indicator that can be used is the frequency of oscillation. From the experimental data, the frequency of oscillation can be found by a Fast Fourier Transform (FFT) of the time-domain data of some state variable (here the pressure). For the model, the frequency can be found from the imaginary part of the pole which has a real part of zero. This pole will be of the form: $s = \pm i\omega_0$, were ω_0 is the angular frequency of oscillation. The frequency of oscillation for the model is therefore given by: $f = \omega_0/(2\pi)$.

It was already stated that the feedback gain was proportional to the temperature gradient along the heat exchanger for the LTP model and proportional to the power input along the heat exchanger for the DHX model. Therefore, the value of the temperature gradient (dT/dy) for the LTP model can be found by using the definition of the feedback gain given in equation

2.21. Using the calculated feedback gain for marginal stability, this will yield the temperature gradient as follows,

$$\frac{dT}{dy} = k\rho_w g \left(\frac{dT}{dP}\right)_{sat} \tag{2.37}$$

Similarly, the power input gradient for the DHX model is found using equation 2.25,

$$\frac{d\dot{Q}_{hx}}{dy} = k_{DHX}\rho_w g \rho_{g,0} T_0 \Delta s_{fg} C_{hx} \tag{2.38}$$

The final performance indicator that will be used is the exergy efficiency. Note that the exergy efficiency can only be defined for the load models, since the no-load models don't have a power generating component. The exergy efficiency evaluates the ratio of the work output to the potential of the input. For heat engines, the maximum thermal efficiency is the Carnot efficiency. Therefore, the exergy efficiency can be seen as the ratio of the thermal efficiency and the Carnot efficiency [14]. For the ERPE, the exergy efficiency is defined as the time-averaged ratio of the work dissipated in the load over the exergy flowrate into the engine from the heat exchanger. The exergy efficiency is thus given by,

$$\eta_{ex} = \frac{\overline{P_{lo,1}(t)U_{lo,1}(t)}}{\overline{T_{hx}(t)\dot{S}_{th}(t)}} = \frac{\overline{P_{lo,1}(t)U_{lo,1}(t)}}{\overline{P_{hx}(t)U_{th}(t)}} \tag{2.39}$$

By using that the pressure and the volumetric flowrate are purely sinusoidal, this can be evaluated to be,

$$\eta_{ex} = \left|\frac{P_{lo,1}}{P_{hx}}\right|^2 \frac{Re(1/Z_{lo,1})}{Re(1/Z_{tot})} = \left|\frac{U_{lo,1}}{U_{hx}}\right|^2 \frac{Re(Z_{lo,1})}{Re(Z_{tot})} \tag{2.40}$$

were $Re(Z)$ denotes the real part of the impedance and the transfers functions $P_{lo,1}/P_{hx}$ and $U_{lo,1}/U_{hx}$ can be found using Kirchoff's current and voltage laws as before.

3 Results and discussion

This chapter presents the results of the ERPE models, of which the modelling was described in the previous chapter. The results of the model are compared with the experimental results, which were acquired using the ERPE prototype. At first these experimental results are described and presented in section 3.1. After that, the results of the ERPE model are given and compared with the experimental results, to attempt to validate the model. This will be done in section 3.2. Finally, a parametric study for the ERPE model will be presented in section 3.3.

3.1 Experimental results

The experimental results of an ERPE prototype were acquired using an experimental set-up at the Boreskov Institute of Catalysis in Novisibirsk, Russia. There is some collaboration between the work done in Russia and at Imperial College London, but not enough to have a big influence on the experimental results. The current work thus has to take the experimental results for granted, and use it for as far as possible. That being said, it was clear from examining the experimental results that not all data was reliable, as will be explained further on.

In total six data sets are available, three sets for the engine without a load and three sets for the engine with a load. The no-load experiments were performed at back-pressures of 3.6 bar, 5.5 bar and 8.2 bar. In this case the pressure at the bottom of the displacer cylinder was recorded for a sufficient amount of time. The load experiments were performed at back-pressures of 5.0 bar, 9.0 bar and 22.0 bar. In this case the pressure at the bottom of the displacer cylinder, before the load and after the load were recorded for a sufficient amount of time. Note that no flowrates were measured during operation of the engine. The flowrates were only measured in a steady flow case, as used in determining the load model in section 2.2.4.

For the experiments with a load, not only the back-pressures were changed between the three experiments, but also the valve setting was altered. Clearly this is unwanted, because multiple parameters were changed between the different experiments, and because of the small amount of data, it is very difficult to pinpoint certain behaviour to specific changes. This is one of the downfalls of the experimental data, and one should take this into account when drawing conclusions about the ERPE model.

For the no-load experiments, the data seems to be under sampled. For all experiments roughly the same sample rate is used to record the pressures. This does not give a problem for the experiments with a load, because the influence of the load is that it lowers the operating frequency of the engine when compared to the no-load case. However, for the no-load experiments, it was clear that during some oscillations a peak or a trough was captured, and in some oscillations no peaks or troughs were detected. This behaviour can be seen from figure 9, were each bullet point represents a data measurement. From this figure it is clear that the peaks and troughs in pressure occur in a very short period when compared to the sample time, and therefore the experiments do not always capture the physical behaviour of the engine. In this case, that is caused because the data is under sampled, which is clear from the fact that the peaks and troughs only consist of one data point.

Frequency identification

To find the operating frequency of the engine for the no-load case, it was not enough to simply perform a Fast Fourier Transform on the time domain data. This method did not shows a clear frequency, especially for the 3.6 bar and 5.5 bar case. Eventually, several methods of acquiring the operating frequency were performed, which all seemed to point to the same frequency within a certain confidence interval. The best method was to apply a median filter on the time domain data and subsequently perform the PWELCH algorithm of MATLAB to transform the data into the frequency domain. Together with the results from the other methods that were used, one can be fairly confident that the frequencies lie around the values presented in table 3.

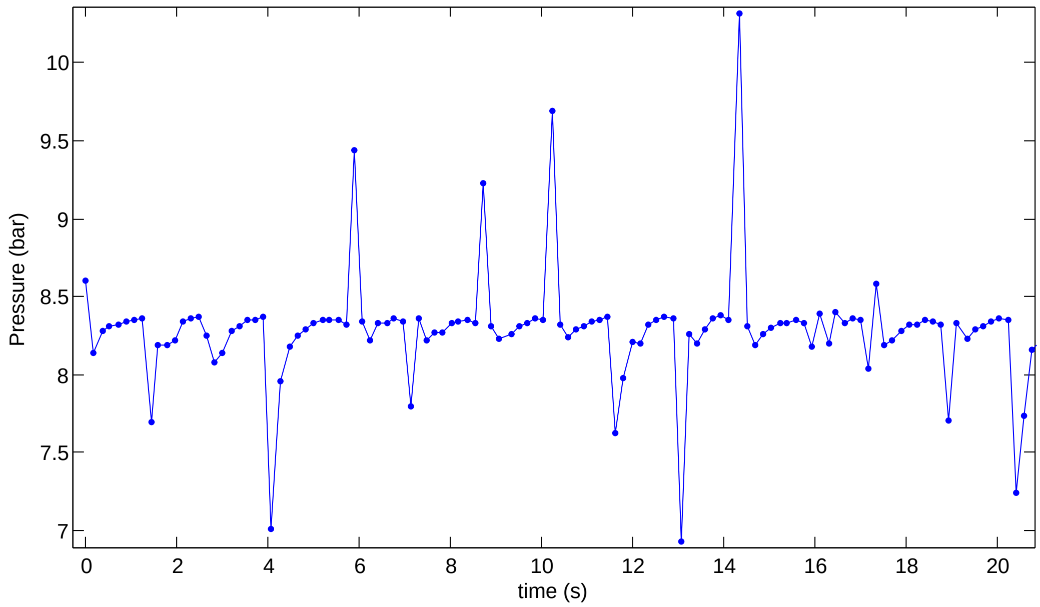

Figure 9: Measured pressure as function of time for the no-load experiment with 8.2 bar back-pressure.

The pressure data for the experiments with a load was significantly better, because the data doesn't seem under sampled. The frequencies could be identified by Fast Fourier Transforms, which resulted in the frequencies presented in table 3.

Table 3: Results of the ERPE prototype experiments

	Frequency (Hz)	dT/dy (K/cm)	d$\dot{Q}$/dy (W/cm)	η_{ex} (%)
3.6 bar (no load)	0.60	40-200	62-310	-
5.5 bar (no load)	0.35	40-200	62-310	-
8.2 bar (no load)	0.60	40-200	62-310	-
5.0 bar (load)	0.017	40-200	36-180	0.1
9.0 bar (load)	0.24	40-200	36-180	0.5
22.0 bar (load)	0.15	40-200	36-180	2.1

Experimental dT/dy and d$\dot{Q}$/dy

It is quite straightforward to acquire the dT/dy from the feedback gain of the LTP model and the d$\dot{Q}$/dy from the feedback gain of the DHX model. Because these performance indicators give insight into one of the most complicated parts of the model, i.e. the heat exchanger, it is interesting to see how the modelled values compare to the experimental values. However, these values are not directly measured in the experimental set-up, so they have to be estimated from available data. This can be done by using the measured temperatures on the outer wall of the hot heat exchanger, the dimensions of the engine and the available data on the flowrates through the catalytic heater. It should be noted that these values were not measured during every experiment, which results in the same values of dT/dy and d$\dot{Q}$/dy for different experiments.

The temperature of the outside of the hot heat exchanger is measured on the top and the bottom of the wall. Next to that, the temperature of the cooling water of the cold heat exchanger has also been measured. This yields a temperature difference of about 600 K between the hot heat exchanger and the cold heat exchanger. Because not much is known about the actual position of the piston in the engine, and therewith the position of the working fluid on top of the piston, it can only be estimated along which length the temperature difference is established. Using the design of the engine, this length is estimated to be between 3 cm and 15 cm. Therefore, the temperature gradient on the outer wall is estimated to be between: $(dT/dy)_{outer} = 40 - 200$ K/cm. To compare the temperature gradient with the ERPE model, the temperature on the inside of the wall should be known. Since no data for the inside of the wall is known, the temperature gradient is assumed to be equal to the one along the outside of the wall. The actual temperatures will be lower on the inner wall, but the temperature gradient could be quite the same. It is worth noting, though, that this estimation is probably an upper estimate, because the temperature gradient is believed to be lower due to the operation of the engine and the direct transport of heat from the hot heat exchanger to the cold heat exchanger. To summarize, dT/dy is estimated to be between 40-200 K/cm for all six experiments, as is shown in table 3.

The value for d$\dot{Q}$/dy can be estimated from the temperatures of the inlet and outlet of the catalytic heater, and the flowrates in it. The catalytic combustion of the propane-butane mixture yields a specific energy input, where it is assumed that complete combustion has occurred. By calculating the enthalpy difference of the inlet and outlet streams, together with the energy supplied by the reaction, it can be estimated how much energy is transported into the engine. This calculation assumes that all of the unaccounted energy has been transported through the hot heat exchanger into the engine. Using this method, the amount of heat transported into the engine is estimated to be: $\dot{Q}_{total} = 270$ W for the load case and $\dot{Q}_{total} = 465$ W for the no-load case. The length along which this heat input occurs is again unknown, but it is known that this input only occurs at the hot heat exchanger. The estimated length of 3 cm to 15 cm for the estimation of dT/dy was along the full length of the heat exchanger, so the length along the hot heat exchanger is estimated to be half of that, i.e. between 1.5 cm and 7.5 cm. Using that the power input gradient is linear along the heat exchanger wall, the power input gradient is estimated to be between: d$\dot{Q}$/dy = 36-180 W/cm for the load case and d$\dot{Q}$/dy = 62-310 W/cm for the no-load case. This result is also depicted in table 3.

Experimental exergy efficiency

To calculate the exergy efficiency from the experimental data, first the thermal efficiency is calculated. The thermal efficiency is then divided by the carnot efficiency, which in the case of a heat engine, then results in the exergy efficiency.

The thermal efficiency is calculated by dividing the work gained at the load by the power input at the heat exchanger (270 W for the load case). The work gained at the load is calculated by integrating the pressure difference across the load, multiplied with the volumetric flowrate, over one cycle. This result is then divided by the sample time to acquire the average work output of the load. Note that the volumetric flowrates haven't been measured, so they were reconstructed from the pressure data and the load model given in section 2.2.4 by, $U = P/Z_{lo,1}$.

The Carnot efficiency (η_c) is calculated by using $T_h = 600 + 273K$ and $T_c = 20 + 273K$ to yield a Carnot efficiency of:

$$\eta_c = 1 - \frac{T_c}{T_h} \tag{3.1}$$

When dividing the thermal efficiency by the Carnot efficiency, the exergy efficiencies for the different load cases were acquired. The results of these calculations can be seen in table 3.

3.2 Model validation

In this section, the results of the ERPE models will be compared with the experimental results. The experimental results, as presented in section 3.1, show some uncertainty in the performance indicators, especially for the gradients dT/dy and d$\dot{Q}$/dy and the frequencies of the no-load case. Next to that, the ERPE model is a linearized model, whilst there is clearly some non-linear behaviour in the physical design of the engine, e.g. the piston valve. When combining these aspects, it is clear that the validation of the model should only be done by checking whether the performance indicators are in the correct order of magnitude. Any more specific conclusions should not be drawn, because of the uncertainty in the experimental results. Next to the one on one comparison between the model and the experimental results, it is also interesting to check whether the model shows the same trends in the performance indicators with changing set-up conditions, such as the back-pressure.

3.2.1 No-load models

At first the models without a load are compared with the experimental results. For this purpose, both the LTP and DHX models were solved for the three different back-pressures, namely: 3.6 bar, 5.5 bar and 8.2 bar. In these calculations, the change of the nominal values of the electrical parameters with different back-pressure has been taken into account. The change of these parameters, with changing back-pressure, can be found in table A2 in appendix A.

No-load frequency
The first performance indicator that will be examined for the no-load models is the frequency. The results from the experiments, the LTP model and the DHX model can be seen in table 4. From these results it is clear that both models overestimate the frequency in every case. The LTP model seems to be about one order of magnitude too high, while to DHX model approaches the experimental values significantly better, albeit still too high.

Both the LTP model and the DHX model show an increasing frequency with increasing back-pressure. It is, however, hard to validate whether this behaviour is correct because the experimental data doesn't show any linear trend with changing back-pressure. To identify whether this estimated trend is correct, new, and more reliable, experiments should be done. This will show whether this trend is actually physical behaviour, or just behaviour inherent of the models.

Table 4: Frequency of the ERPE models and experiments for the no-load case

	Experiments	LTP model	DHX model
3.6 bar	0.6 Hz	5.0 Hz	2.3 Hz
5.5 bar	0.35 Hz	7.3 Hz	2.8 Hz
8.2 bar	0.6 Hz	8.5 Hz	3.2 Hz

No-load gradients
The remaining performance indicators are the values of dT/dy for the LTP model and the values of d$\dot{Q}$/dy for the DHX model. Note that there are no efficiencies in the no-load models, since there is no means of power generation to define an efficiency with. The results for the gradients of the models, as well as the results from the experiments, are shown in table 5.

It is clear from table 5 that the values for dT/dy of the LTP model are in the correct order of magnitude, especially the values for 5.5 bar and 8.2 bar back-pressure. When looking at these temperature gradients individually, however, they are definitely too high in a physical sense. For example, a dT/dy of 636 K represents a temperature difference of 1908-9540 K between the heat source and heat sink, which is too high for almost any physical system, and definitely too high for the current engine. Next to the individual values, there doesn't seem to be a linear trend in the temperature gradients of the LTP model with changing back-pressure. Remember that no trends can be seen from the experimental results as well, because these are 'constant' for every back-pressure, as explained in section 3.1.

The values for d$\dot{Q}$/dy of the DHX model are at least two orders of magnitude too high in every case. These power inputs are clearly too high in a physical sense, and it shows that the DHX model for no load isn't able to approximate the behaviour of the ERPE. Next to that, the values increase with increasing back-pressure. This trend could still represent the actual behaviour of the engine, but this can't be confirmed due to the absence of enough experimental results.

Table 5: Gradients of the ERPE models and experiments for the no-load case

	Experimental dT/dy (K/cm)	LTP dT/dy (K/cm)	Experimental d$\dot{Q}$/dy (W/cm)	DHX d$\dot{Q}$/dy (W/cm)
3.6 bar	40-200	636	62-310	1.2e4
5.5 bar	40-200	310	62-310	2.6e4
8.2 bar	40-200	344	62-310	5.2e4

To summarize, the DHX model performs better in predicting the operating frequency of the engine than the LTP model. Both models predict a frequency that is too high, but they are quite close to the experimental results. One thought of lowering these frequencies in the model is to add thermal losses, which hasn't been done in the current model. These thermal losses, which are definitely present in the physical system, are thought to lower the predicted frequencies closer to the observed values.

A comparison of the gradients along the heat exchanger can't be done between the LTP model and the DHX model, because they both predict different things. It can, however, be said that the LTP model predicts values that are way more realistic than the DHX model does.

3.2.2 Load models

In this section, the models with a load are compared with the experimental results. For this purpose, both the LTP and DHX models were solved for the three different back-pressures, namely: 5.0 bar, 9.0 bar and 22.0 bar. In these calculations, the change of the nominal values of the electrical parameters with different back-pressure has been taken into account. The change of these parameters, with changing back-pressure, can be found in table A2 in appendix A. As already mentioned before, not only the back-pressure was changed between these three experiments, but also the setting of the load valve was altered. It was attempted to model this behaviour using three different load models. It is known from the experiments that the highest resistance of the valve was set for the 5 bar back-pressure case, and the lowest resistance for the 22 bar back-pressure case. In the latter case, it was reported that the valve was almost completely open, and was thus almost simulating a no-load case.

Frequency including load

The first performance indicator that is examined is the operating frequency of the engine. The results for the experiments, the LTP model and the DHX model can be seen in table 6. From these results it is clear the LTP model overestimates the frequency by two to three order of magnitude. When compared to the no-load case, the experimental frequencies dropped significantly, whilst the frequencies of the LTP model have increased. So the frequencies aren't only way too high, but they also tend to change in the wrong direction. From this it is clear that the LTP model isn't able to predict the operating frequency of the ERPE for the load case. Next to that, the trend of increasing frequency with increasing back-pressure, as predicted in the no-load case, isn't present anymore for the LTP model with the load.

When comparing the predicted frequencies of the DHX model with the experimental data, it is clear that the DHX model performs really well. Especially for the 5 bar and 9 bar back-pressure case, the predicted frequency is in the same order of magnitude and fairly close to the experimental values. Only for the 22 bar case the predicted frequency is too high, albeit in the same order of magnitude. This could be caused by the fact that the load valve was almost completely open in the 22 bar case, which makes it approach the no-load case, were the predicted frequencies were all too high (see table 4). Finally, it's worth noting that the DHX model still has the trend of increasing frequency with increasing back-pressure. The experimental data doesn't show this trend, so it is unclear whether this behaviour is correct. However, considering that the 22 bar case is almost a no-load case, the DHX model does predict the jump in frequency between the 5 bar and 9 bar case, as shown from the experimental results. This might show that the DHX model correctly predicts the trend in frequency as function of back-pressure, but more data is needed to verify this property.

Table 6: Frequency of the ERPE models and experiments for the load case

	Experiments	LTP model	DHX model
5.0 bar	0.017 Hz	20.4 Hz	0.04 Hz
9.0 bar	0.24 Hz	9.9 Hz	0.13 Hz
22.0 bar	0.15 Hz	10.1 Hz	1.02 Hz

Gradients including load

In this section the predicted gradients along the heat exchanger, from the LTP model and the DHX model, are compared with the experimental results. The values for the experiments, the LTP model and the DHX model can be seen in table 7. From this table it is clear that the predicted temperature gradient along the heat exchanger in the LTP model is way too high. For the 5 bar case, the estimated temperature gradient is 5 orders of magnitude too high, which is pure nonsense. This temperature gradient means that either the temperature of the entire engine has to be extremely high (millions of degrees Kelvin), or the temperature of the cold heat exchanger has to be way below absolute zero, which are both highly unphysical. It is seen, however, that the predicted gradients become more realistic with increasing back-pressure. This might be caused by the fact that the resistance of the valve was lowered with increasing back-pressure, thus moving towards a no-load case. This seems to cohere with the no-load results, were the predicted temperature gradients were in the correct order of magnitude. That being said, for every load case, even for the 22 bar case, the predicted temperature gradients are way too high and completely unrealistic.

The results for the power input gradient of the DHX model are in the correct order of magnitude, although a bit too high. This is, however, a dramatic improvement from the no-load model, were the predicted power input gradient was way too high. It is also clear from the results that the predicted power input gradient increases with increasing back-pressure and smaller valve resistance. This results in a unrealistic value for the 22 bar case, which is quite close to the no-load case, which all predicted a way too high power input gradient (see table 5). However, the 5 bar and 9 bar case show that the DHX model is able to predict the power input gradient for load cases quite well.

Table 7: Gradients of the ERPE models and experiments for the load case

	Experimental dT/dy (K/cm)	LTP dT/dy (K/cm)	Experimental d$\dot{Q}$/dy (W/cm)	DHX d$\dot{Q}$/dy (W/cm)
5.0 bar	40-200	3.8e7	36-180	157
9.0 bar	40-200	4.3e5	36-180	223
22.0 bar	40-200	1.0e4	36-180	7145

Exergy efficiency including load

The final performance indicator that is investigated is the exergy efficiency. The results from the experiments, the LTP model and the DHX model can be seen in table 8. From these results it is clear that the predicted efficiency of the LTP model is orders of magnitude too low for the 5 bar and 9 bar case. For the 22 bar case the efficiency is about one order of magnitude too low, but since this is the case were the load valve is almost completely open, it is also the case which one should look at the least. Therefore, it can be concluded that the LTP model performs poorly when predicting the exergy efficiency of the engine. This conclusion might very well be coupled with the predicted gradients of the LTP model, because these were extremely high. These extremely high gradients represent a high energy input into the system, and therefore the acquired energy in the load also has to be enormous to get a significant efficiency. Finally, for what it's worth, it should be noted that the LTP model does predict the same increasing trend in exergy efficiency with increasing back-pressure.

For the 5 bar and 9 bar case the DHX model overestimates the efficiency by about one order of magnitude. For the 22 bar case the efficiency is about one order of magnitude too low. The difference in this behaviour can be explained by the fact that for the 22 bar case the load valve was almost completely open. One should therefore mainly look at the 5 bar and 9 bar case. The overestimation of the efficiency could be explained by the fact that no thermal losses have been modelled. The higher efficiencies for the DHX model were also predicted in the previous work on the NIFTE, which were subsequently corrected by introducing thermal losses in the system [16]. Due to the analogy in the modelling, it is therefore expected that introducing thermal losses in the ERPE framework might also correct the efficiencies up to the correct order of magnitude. Finally, it should be noted that the DHX model does not capture the trend in exergy efficiency with changing back-pressure, as given by the experimental results. The DHX model actually predicts an opposite trend.

Table 8: Exergy efficiency of the ERPE models and experiments for the load case

	Experiments	LTP model	DHX model
5.0 bar	0.1 %	4.5e-5 %	10.4 %
9.0 bar	0.5 %	4.4e-3 %	7.7 %
22.0 bar	2.1 %	0.2 %	0.3 %

To summarize, the LTP model doesn't predict any of the performance indicators to be in the correct order of magnitude. For the most important cases, i.e. the 5 bar and 9 bar case, the predictions differ multiple orders of magnitude from the experimental data. From this, it can be concluded that the LTP model performs very poorly for the models with a load.

The DHX model performs quite well for all three performance indicators. The 22 bar case shows the most deviation when compared with the experiments, but as explained, this is also the case one should look at the least. When looking at the 5 bar and 9 bar case only, the frequency is predicted really well. Next to that, the power input gradient and the exergy efficiency are slightly overestimated. Overall, it can be concluded that the DHX model performs quite well for the models with a load.

3.3 Parametric study

The purpose of this parametric study is to check the influence of changing all the electrical parameters on the performance indicators. Some of these electrical parameters only depend on the design of the engine, and some on the design and the operating conditions of the engine. By gaining an understanding of how the electrical parameters change the performance indicators, one can predict how a change in design or operating conditions of the actual engine will change its performance. Therefore, the parametric study can be used to optimize the ERPE design and its operating conditions as a function of the performance indicators. In this section, however, only the influence of the parameters on the performance indicators is examined, so no optimization will be carried out. This is not done because the confidence in the linear model isn't great, especially when trying to predict trends in the performance indicators. Therefore, this parametric study should only be seen as a first indication of the dependence of the performance indicators on the electrical parameters.

In this study, only the 5 bar and 9 bar case for the DHX model with a load will be examined. It is chosen to only look at a model with a load, because the actual engine will also house a load. Next to that, the 5 bar and 9 bar case of the DHX model were the only two cases were enough resemblance between the model and the experiments was found to be confident about the validity of the model (see section 3.2). The other models and cases are thus not examined, because it seems of no use to perform a parametric study on a model which can not predict the behaviour of the engine anyway.

The parametric study is performed by changing one of the electrical parameters, whilst keeping the other parameters at their nominal values. The investigated range is three, and sometimes four, orders of magnitude above and below the nominal value of the parameter. The nominal values of the electrical parameters, as function of back-pressure, are given in table A2 in appendix A.

The parametric study showed that most electrical parameters do not have a significant influence on the performance indicators. The results for these parameters will not be given in this report, because no interesting conclusions can be drawn from these results. One has to keep in mind, however, that it is also an important result if a parameter does not change the performance indicators much. This gives the designer the freedom to alter the physical components, represented by the parameters, without changing the performance of the engine much. This could prove to be useful for designing and construction purposes.

Four parameters are found which do have a significant influence on at least one of the performance indicators. These four parameters are: C_{hx}, R_{th}, C_{vd} and C_{ld}. Each of these parameters will be treated in their own section, where the physical representation of the parameter will be explained and the influence on the performance indicators will be given. Note that, for clarity of the report, not all corresponding figures will be presented in these sections. Most figures will be given in appendix C, but all conclusions drawn from these figures are given in the main report.

Influence of C_{hx}

The electrical capacitance C_{hx} represents the capacity to store and release energy from the heat exchanger wall. Its definition, and therewith the physical properties it depends on, can be seen in table 1 in section 2.2.3.

The most interesting influence of C_{hx} is on the power input gradient. The results for the power input gradient of the 5 bar and 9 bar case are depicted in figure 10. Note that the 5 bar and 9 bar case were both investigated by calculating the results up to three orders of magnitude above and below their nominal values, but that the nominal values between the two cases differ. Therefore, in a non-normalized plot for C_{hx}, one of the plots would be shifted with respect to the other (in this case the 9 bar plot to the right). It should be kept in mind that this same effect will be present in all figures depicted in this section and appendix C.

An interesting result, as shown in figure 10, is that the power input gradient is almost at its minimum for the nominal C_{hx} of the 5 bar case. Since the predicted power input gradients were slightly too high (see table 7), it would have been interesting too see for which value of C_{hx} the power input gradient would be correct. For the 5 bar case, however, this situation can not be acquired by changing C_{hx}. In contrast to that, the 9 bar case shows that the power input gradient can still be significantly decreased with increasing C_{hx}. Next to that, the 9 bar case also rises again after the minimum around $C^*_{hx} \approx 10^2$, albeit way slower than the 5 bar case. Finally, both the 5 bar and 9 bar case show that the required power input gradient becomes significantly higher when decreasing the capacitance of the heat exchanger wall to store and release energy.

Next to the power input gradient, the value of C_{hx} also has a significant influence on the other two performance indicators. The influence of C_{hx} on the operating frequency can be seen in figure C2 in appendix C. This figure shows that, for the 9 bar case, raising C_{hx} will decrease the frequency and decreasing C_{hx} will raise the frequency. For the 5 bar case, figure C2 shows that decreasing C_{hx} also raises the frequency, but that increasing C_{hx} almost has no influence on the frequency. It seems that the operating frequency as function of C_{hx} is almost at its

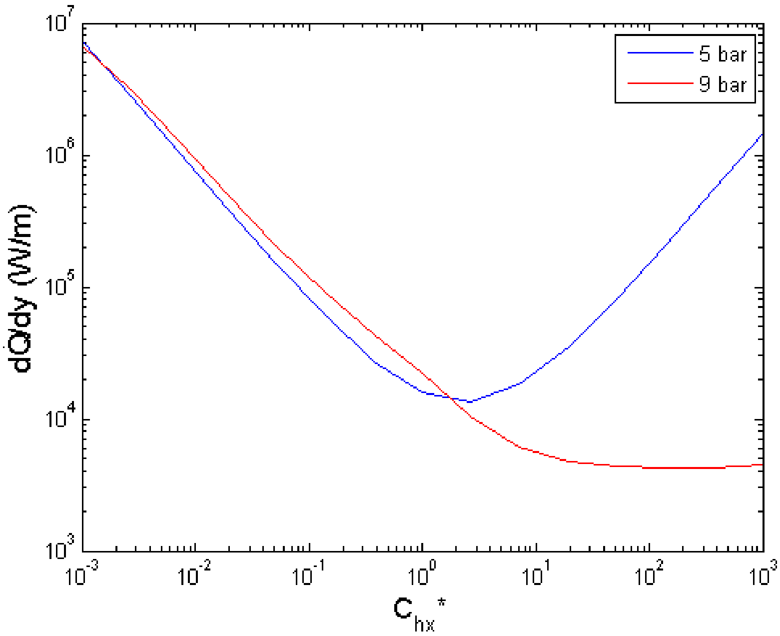

Figure 10: Parametric study: Power input gradient as function of C_{hx}, where C_{hx}^* is the normalized value for C_{hx}. Note that the nominal value of C_{hx} is different for the 5 bar case (blue) and the 9 bar case (red).

minimum for the 5 bar case.

Finally, the influence of C_{hx} on the exergy efficiency can be seen in figure C1 in appendix C. This figure shows that the exergy efficiency is almost at its maximum, but that it can be slightly increased by raising C_{hx} for both the 5 bar and 9 bar case. Next to that, it can be seen that the 9 bar case can result in a higher efficiency than the 5 bar case. For a value of C_{hx} lower than the nominal value, the 5 bar and 9 bar case are very much alike, and they show that the exergy efficiency keeps dropping with decreasing C_{hx}.

Influence of R_{th}

The electrical resistance R_{th} is a measure of the thermal resistance for heat flow through the heat exchanger. Its definition, and therewith the physical properties it depends on, can be seen in table 1 in section 2.2.3.

The value of R_{th} significantly influences all three performance indicators. Its influence on the operating frequency is shown in figure 11. From this figure it is clear that increasing the thermal resistance decreases the operating frequency, which seems to be a physically correct result, since a higher resistance tends to slow things down in general. Inversely, decreasing the thermal resistance increases the operating frequency. Next to that, the operating frequency seems to be significantly higher for the 9 bar case, when compared to the 5 bar case, over the entire investigated range. This could be caused by the increased back-pressure, but it is probably caused by the lowered resistance of the load valve for the 9 bar case.

The influence of R_{th} on the power input gradient can be seen in figure C3 in appendix C. From this figure it is clear that decreasing the thermal resistance increases the power input gradient for both cases. When increasing the thermal resistance, the power input gradient for the 5 bar case keeps dropping, whilst for the 9 bar case it seems to asymptotically tend to a constant value.

The influence of R_{th} on the efficiency can be seen in figure C4 in appendix C. First of all, it is clear from this figure that the exergy efficiency is quite unstable with respect to changes in

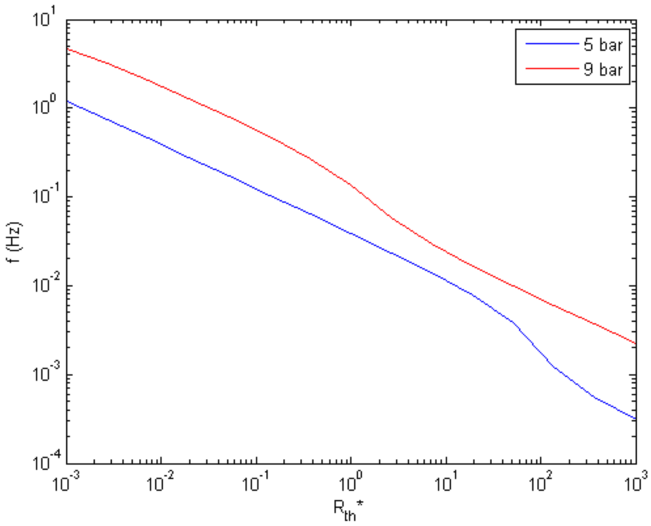

Figure 11: Parametric study: Frequency as function of R_{th}, where R^*_{th} is the normalized value for R_{th}. Note that the nominal value of R_{th} is different for the 5 bar case (blue) and the 9 bar case (red).

R_{th}, especially for the 5 bar case, and it is therefore hard to draw conclusions about the trends with changing R_{th}. Both cases seem to have a decreasing efficiency with increasing R_{th}. Next to that, the 5 bar case shows an almost constant efficiency for thermal resistances lower than the nominal value, whilst the 9 bar case shows an increase in efficiency.

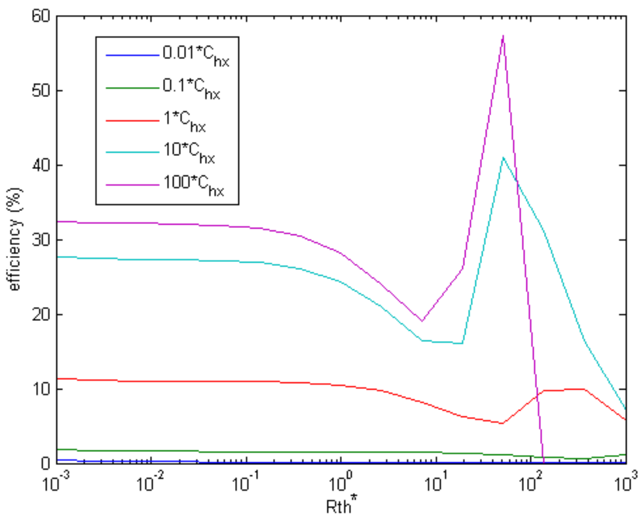

Figure 12: Parametric study: efficiency as function of R_{th} for five values of C_{hx}, where R^*_{th} is the normalized value for R_{th}. Note that this figure only depicts the 5 bar case.

To gain more insight into the strange behaviour of the efficiency with a R_{th} higher than the nominal value, a plot has been made which depicts the efficiencies as function of R_{th} for five different values of C_{hx}, see figure 12. From this figure it is clear that the strange behaviour seen in figure C4 was not random, but that multiple cases show a peak in efficiency for thermal resistances higher than the nominal value. This behaviour is greatly increased for increasing values of C_{hx}. Due to a lack of experimental results, it is not clear whether this behaviour is physical or just a consequence of the modelling technique. However, due to the enormous spike in efficiency, it is at least worth investigating in future work.

Influence of C_{vd}

The electrical capacitance C_{vd} represents the capacitance of the gas spring on top of the displacer cylinder. Note that the derivation for the gas spring, albeit the one for the working cylinder, has been done in section 2.2.1. The definition of C_{vd}, and therewith the physical properties it depends on, can be seen in table 1 in section 2.2.3.

Changes in C_{vd} from its nominal value significantly change all three performance indicators. The most interesting one, the change of the power input gradient with varying C_{vd}, is shown in figure 13. The change in power input gradient by changing C_{vd} is very similar to the behaviour of varying C_{hx}, as was depicted in figure 10. For the 5 bar case the nominal value seems to be almost at the minimum power input gradient, and raising or lowering C_{vd} significantly increases the power input gradient. The 9 bar case also increases significantly with decreasing C_{vd}, but the power input gradient only slightly increases with increasing C_{vd}, after having a minimum around $C^*_{vd} = 10^{1.5}$. Once again the similarity with the C_{hx} variation is pointed out, because this seems to be an interesting result. The similarity might be caused because both parameters represent a capacitance in the top part of the physical engine. However, in the electrical (RLC) circuits the capacitances are not placed in series, so this result is not trivial and indeed quite remarkable.

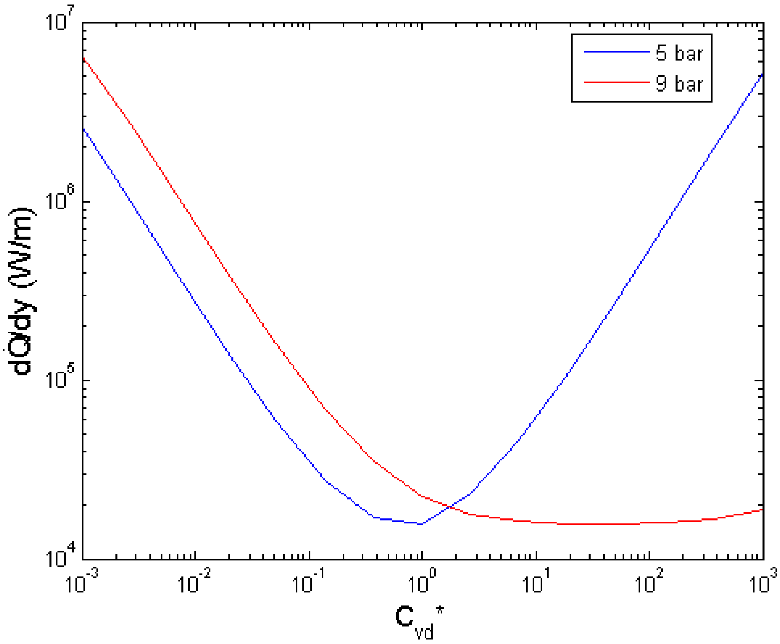

Figure 13: Parametric study: Power input gradient as function of C_{vd}, where C^*_{vd} is the normalized value for C_{vd}. Note that the nominal value of C_{vd} is different for the 5 bar case (blue) and the 9 bar case (red).

The influence of varying C_{vd} on the frequency can be seen in figure C5 in appendix C. This figure is again really similar to the case in which C_{hx} was varied, as depicted in figure C2. The main difference is that the frequencies are slightly shifted in height and that the 9 bar case is an even straighter line.

Finally, the influence of varying C_{vd} on the exergy efficiency is shown in figure C6 in appendix C. Surprisingly enough, the exergy efficiency does not show the same behaviour as in the

C_{hx} case (see figure C1), it actually shows the opposite behaviour. When increasing C_{vd}, the exergy efficiency significantly drops, where the gradient for the 5 bar case is steeper than for the 9 bar case. Next to that, for lower values of C_{vd}, the exergy efficiencies rise to enormously high values, especially for the 5 bar case. In this case, the exergy efficiency is predicted to rise above 90 percent, which seems to be an unrealistic value. However, the trend of increasing efficiency might be correct, and it is therefore interesting the investigate this behaviour in future work.

Influence of C_{ld}

The electrical capacitance C_{ld} represents the capacitance of the liquid column in the displacer cylinder, which can be seen as the hydrostatic capacitance. The definition of C_{ld}, and therewith the physical properties it depends on, can be seen in table 1 in section 2.2.3.

In contrast with the other three parameters, varying C_{ld} only had a significant effect on one of the performance indicators, namely the power input gradient. The results on the power input gradient for varying C_{ld} can be seen in figure 14. The results are quite straightforward. Both cases show an increasing power input gradient for increasing C_{ld} and a decreasing power input gradient for decreasing C_{ld}. In fact, both cases show an almost perfect linear relation between C_{ld} and the power input gradient in the logarithmic domain. This can be called a remarkable results, since this has not been so clearly present in the other cases. Finally, it is noticed that the 9 bar case has an approximately 50 percent higher power input gradient for the entire investigated range.

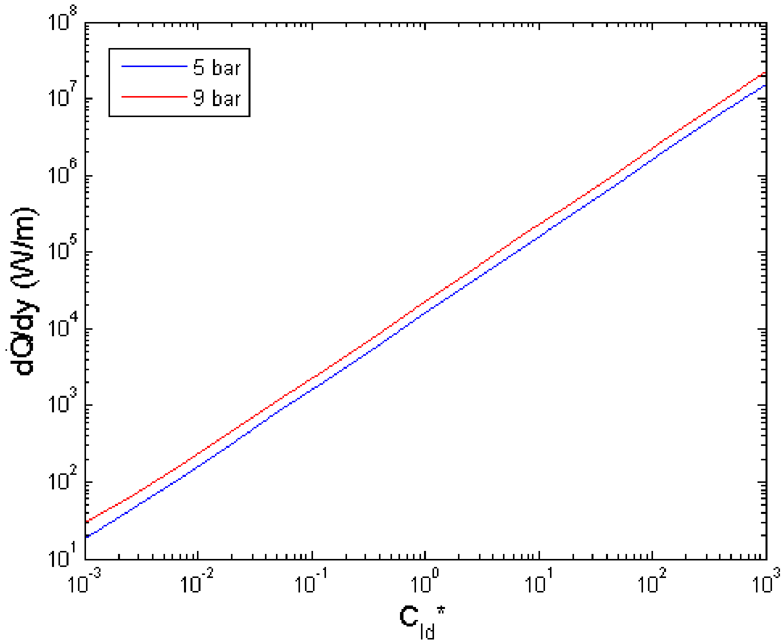

Figure 14: Parametric study: Power input gradient as function of C_{ld}, where C_{ld}^* is the normalized value for R_{th}. Note that the nominal value of C_{ld} is different for the 5 bar case (blue) and the 9 bar case (red).

The influence of C_{ld} on the exergy efficiency can be seen in figure C7 in appendix C. As already mentioned, the influence is insignificant. From the nominal value of C_{ld} and higher, the efficiency doesn't change. Only around two orders of magnitude lower than the nominal C_{ld} the efficiency starts dropping a bit. One interestig thing than can be seen from figure C7 is that the 5 bar case has an exergy efficiency which is around 3 percent higher than the 9 bar case throughout the entire investigated range.

Finally, it is noted that there was as good as no change in the frequency with changing C_{ld}, therefore these results were omitted. However, just as mentioned in the beginning of this section, the fact that a parameter does not influence a certain performance indicator, does not mean that it is not an interesting result. For example, in the current case of varying C_{ld}, it is clear that only the power input gradient is significantly influenced. This means that a designer can change the value for the power input gradient, whilst keeping the other performance indicators unaltered.

4 Experiments

This chapter will describe the experiments that have been performed in light of this work. At first the motivation for doing these experiments is given in section 4.1. Subsequently, the design of the experimental set-up and the way in which it should lead to the wanted results, is explained in section 4.2. Finally, the results of the experiments are given and then discussed in section 4.3.

4.1 Motivation for the experiments

The previous results, and especially the results from the model validation part in section 3.2, have shown that the linear model has quite some downfalls in predicting the behaviour of the actual physical engine. The main cause of these downfalls is thought to be introduced by the linearisation of the problem, whilst there are definitely some non-linear components in the engine. For example, the check valve system at the load and the piston valve which opens and closes during one cycle (see figure 2) are definitely non-linear. Next to that, the heat exchanger is bound to exhibit non-linear behaviour, which could be the cause that the linear modelling framework isn't able to predict the behaviour of the heat exchanger really well.

An obvious way to try to model these components better is to make a non-linear model, as was eventually also done in the NIFTE work [18]. At the current time of writing, a similar non-linear model for the ERPE is being produced. For this model, however, it is not sufficient to state that the temperature gradient or power input gradient along the heat exchanger wall is linear (or whatever form). An actual temperature profile has to be described. The aim of the experiments presented in this work is to identify what the temperature profile looks like in the actual heat exchanger, which can then be modelled as such in the non-linear model. Next to the form of the temperature profile, the second aim is to identify if, and if so how, the temperature profile changes with changing operating conditions. The latter will ensure that the temperature profile for the non-linear model can not only be used for one specific set of operating conditions, but throughout a wide range of operating conditions.

4.2 Experimental set-up

To acquire the temperature profile along the heat exchanger wall, the experimental set-up shown in figure 15 has been constructed. It mainly consists of two cylinders with an internal piston; the driving cylinder and the working cylinder. The driving cylinder is operated using a compressed air supply. The position of the piston of the driving cylinder can be set by using a computer which controls the valve. By moving the driving cylinder, the piston in the working cylinder is forced to move along. Therewith, the oscillating nature of the ERPE engine is simulated by operating the driving cylinder in a sinusoidal manner.

The top of the working cylinder is filled with 3 cm of pentane, which has a boiling point of 36.1 degrees Celcius at 1 bar. The pentane can therewith be evaporated at the hot heat exchanger and condensed at the cold heat exchanger using relatively save temperatures. The purpose of these phase changes is to simulate the same behaviour that the actual ERPE heat exchanger experiences. The cold heat exchanger uses cooling water at around 20 degrees Celcius, whilst the hot heat exchanger is used op to 100 degrees Celcius.

During operation of the engine, the 14 thermocouples facing the back of the working cylinder measure the temperature. Holes of about 3 mm deep, into the 5 mm thick wall of the working cylinder, have been drilled to more accurately measure the temperature inside the wall. For this purpose, the holes where filled with thermal paste as well. The position of the thermocouples along the height of the heat exchanger can be seen in figure 16. It is clear from the set-up that most thermocouples are placed in the region between the hot heat exchanger and the cold heat exchanger, because the highest gradient in temperature is expected here. Finally, the position of the piston through the flux based position sensor, the pressure in the top region of the working cylinder and the temperature at the thermocouples is collected with the data acquisition system. The data is then send to a computer, where the data is stored for later analysis.

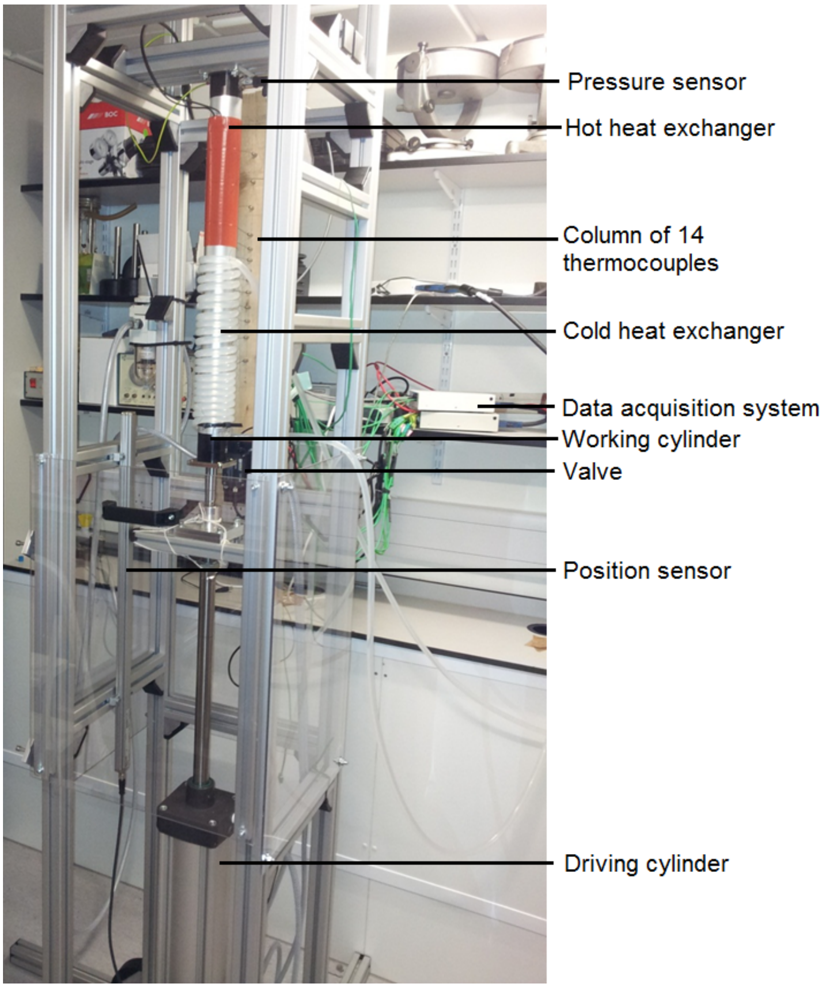

Figure 15: Photograph of the experimental set-up, where the most important components are pointed out and given a name.

To capture the temperature profile for a range of operating conditions, multiple experiments have been done. In these experiments three operating conditions were varied, namely the strokelength of the driving cylinder, the sinusoidal frequency of the driving cylinder and the temperature of the hot heat exchanger. The amplitude of the strokelength has been set to 72 mm and 144 mm, so the total range of the piston was those values doubled. The mean position of the piston is exactly between the hot heat exchanger and the cold heat exchanger, it can therefore be seen from figure 16 what the range of the piston was during these experiments. Next to that, the frequency of the driving cylinder has been set to 25, 50 and 100 mHz. Finally, the temperature of the hot heat exchanger has been set to 70, 85 and 100 degrees Celcius. Making sure that only one variable was varied for each experiment, a total of $2 \cdot 3 \cdot 3 = 18$ experiments have been done. It was made sure that for each experiment at least 25 full oscillations were captured, which showed to be enough for sufficiently accurate results by looking at the time domain data and their Fourier transforms.

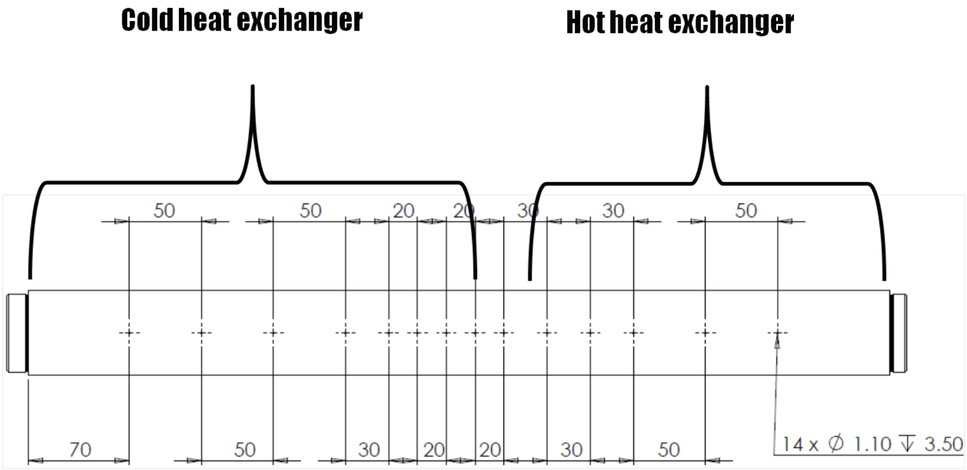

Figure 16: Schematic of the position of the thermocouples along the heat exchanger, where all lengths are given in mm.

4.3 Experimental results

To process and analyse the experimental data quickly, a MATLAB function has been written. This function reads in the experimental data, and then filters it using a low-pass butterworth filter. The latter was needed because there was quite a lot of noise, especially for the thermocouple data, but because the highest oscillation frequency was 0.1 Hz and the sample rate was 1000 Hz, the filtering did not pose any serious problems. After the data has been filtered, the function provides several analysis options, such as plotting a PV diagram, plotting the temperature along the working fluid during one cycle, plotting the change of the temperature profile during one cycle and Fourier transforms to identify the dominant oscillations. These functions are written for further investigation, and are beyond the scope of this document. However, one PV-plot will be shown at the end of this section, just to show that more than the following analysis can be gained from the experimental set-up.

The main interest for this report is a plot of the temperature profile along the heat exchanger, which is also available in the mentioned function. For this purpose, the temperature at all the thermocouples is averaged over one or multiple oscillations, such that a single temperature value per thermocouple is acquired. Notice that this is a slight simplification, because the actual temperature was found to oscillate slightly during one cycle, but not enough to worry about in the current analysis. The temperature amplitude at specific points in the heat exchanger, however, might be interesting to examine in future work.

For one of the 18 experimental cases, the resulting temperature profile is shown in figure 17. Note that both axes have been normalized, which will be elaborated further on. When examining the figure, one can see that the temperature profile looks a bit like the shape of a tanh function. Suspicion is therefore raised whether the temperature profile along the heat exchanger wall could be modelled with a tanh function. For this purpose, one should first get into more detail about the tanh function, which is depicted in figure 18. This figure shows that the tanh function has two parameters, α and β. The parameter α is half of the difference between the maximum and minimum of the tanh function, and therefore α can be seen as the amplitude. With α set, the parameter β then sets the slope of the tanh function at the origin. For comparison, on the left hand side of figure 18 the linear temperature profile, which was used for the LTP model, is shown.

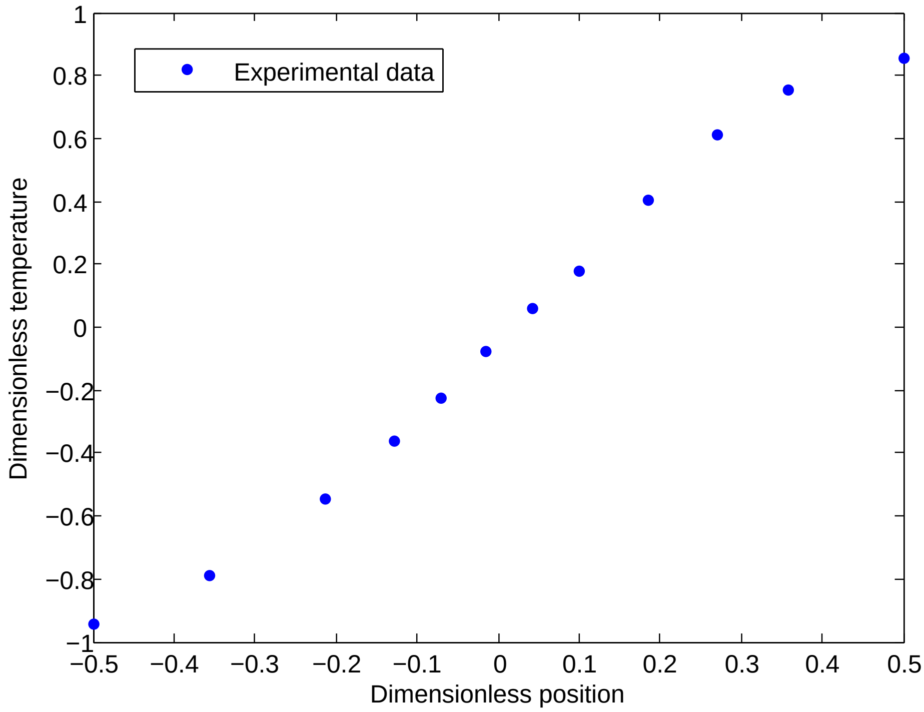

Figure 17: The temperature profile for the case where the hot heat exchanger was set to 100 degrees Celcuis, the oscillating frequency was 25 mHz and the strokelength was 72 mm.

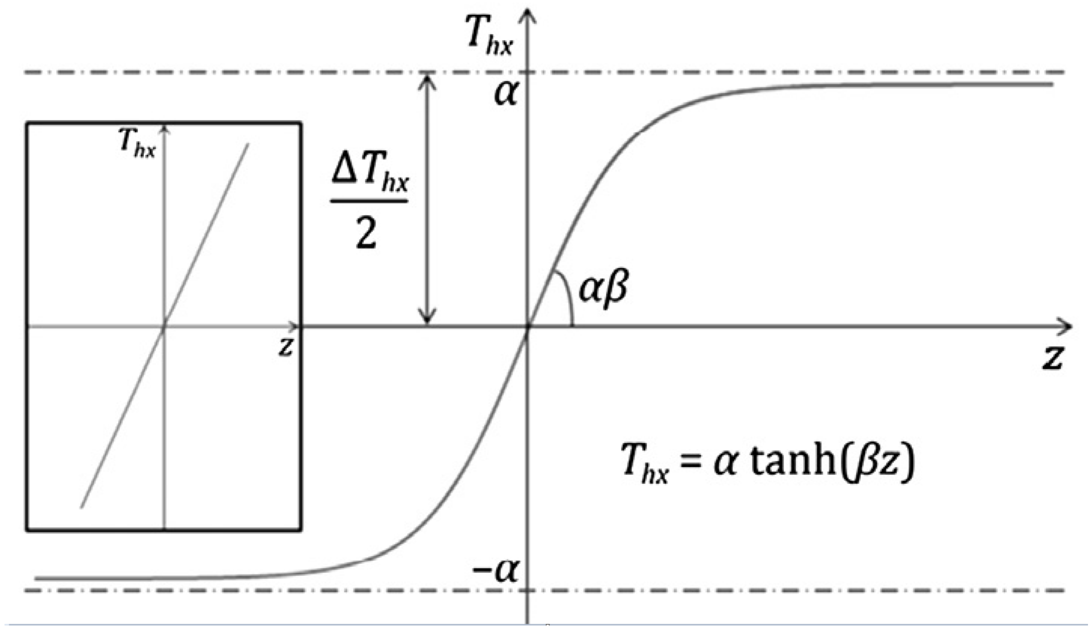

Figure 18: A schematic of a tanh function, where α determines the temperature amplitude and β determines the slope at the origin.

To check whether the temperature profile of the experimental data indeed is given by a tanh function, the experimental data is fitted with a tanh function in MATLAB. First of all, it should be noted that, since the experimental data was normalized between -1 and 1, the value of α is equal to 1. Therefore, the only variable of interest is β. Next to that, the position of the piston has also been normalized, but in this case between -0.5 and 0.5 (which is arbitrary). Because all 18 experiments are normalized in this way, the results for β can be directly compared, even though they might have different positions and temperatures in the non-normalized domain. When trying to fit the tanh function to the normalized experimental data, the result depicted in figure 19 is acquired. Note that this is the same experimental case as in figure 17. The root mean square error for this fit was found to be sufficiently small, as can also be observed from the figure itself, from which it can be concluded that the temperature profile of the heat exchanger can indeed be described by a tanh function quite well. This means that the proposed non-linear model can use a tanh function for the temperature profile, where setting α will set the temperature difference (which might depend on the examined case) and β is determined by the tanh fit with the corresponding experiment. There is one big downfall of this procedure, namely, for each case that one wants to model, there has to be an experiment which predicts β. To elimate this problem, the other 17 experimental cases where also examined, to try and find a relation for the change in β with changing experimental conditions.

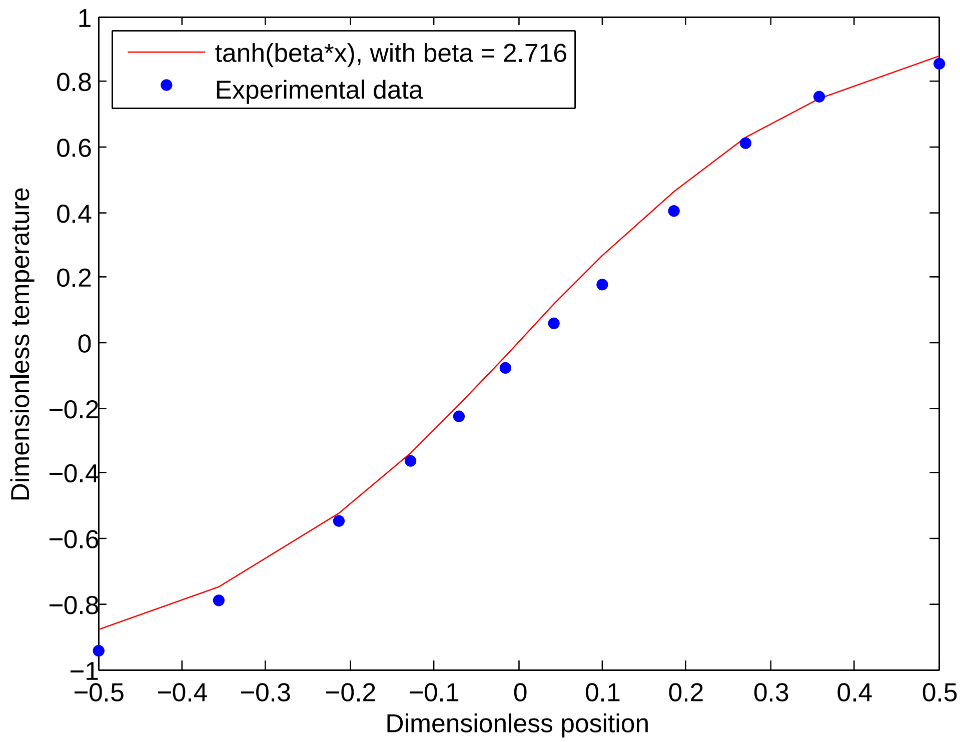

Figure 19: Fit of a tanh function for the experimental results, where the hot heat exchanger was set to 100 degrees Celcuis, the oscillating frequency was 25 mHz and the strokelength was 72 mm.

The same plots, as the one in figure 19, have been made for the other 17 experimental cases as well. From examining these plots it was clear that they were all quite similar, and because the tanh fit only depends on one parameter in the normalized case, it seems of no use to present more (or all) of these figures. The main interesting thing to note about the fits is that, as in the previously shown case, the root mean square errors were found to be sufficiently small. Therefore, all experimental temperature gradients can be approximated by a tanh function quite well. One final point that has to be mentioned is that the approximation for a tanh function seems to be better at the top position than at the bottom position. It is expected that this might not be true in the actual engine, but is mainly caused due to the poor cooling of the silicon tubes in the experimental set-up. For future experiments, it is recommended to improve the cooling, e.g. by using copper tubes.

The value of β for all cases with a strokelength of 72 mm can be seen in table 9. The value of β for all cases with a strokelength of 144 mm can be seen in table 10. After a first look at both tables, it seems that all values of β are fairly close to each other. The highest β is found to be 2.72 for the 25 mHz, 100 °C, 72 mm case and the lowest β is found to be 2.33 for the 100 mHz, 85 °C, 144 mm case. This is a deviation of about 8 % around the mean for the two most extreme cases. All other cases have less deviation around the mean value of β, from which it seems that it is quite a good approximation to use the same value of β for every case that will be modelled. For the first version of the non-linear model, this approximation for β will definitely be good enough, and it is also the easiest way to implement a temperature profile. When averaging all values of β, one can therefore conclude that $\beta = \mathbf{2.56}$ can be used to acquire the temperature profile, for all cases that will be modelled, to a sufficient amount of accuracy. Note however that, the slope at the origin is given by the product of α and β, as can be seen in figure 18. In the normalized case $\alpha = 1$, but for the actual models one chooses an α to set the temperature amplitude, and one probably uses a non-normalized length axis. Therefore, one has to be careful how the normalized value of $\beta = 2.56$ is used to set the angle at the origin of the actual model.

Table 9: Value of β for all frequencies and temperatures, with a strokelength of 72 mm.

72 mm cases	70 °C	85 °C	100 °C
25 mHz	2.67	2.72	2.72
50 mHz	2.61	2.65	2.67
100 mHz	2.58	2.63	2.64

Table 10: Value of β for all frequencies and temperatures, with a strokelength of 144 mm.

144 mm cases	70 °C	85 °C	100 °C
25 mHz	2.54	2.57	2.60
50 mHz	2.45	2.45	2.48
100 mHz	2.35	2.33	2.35

Only for extreme cases, way beyond the cases tested in the experiments, one might have to model specific trends in β for changing operating conditions. For future models, which might want to implement these trends, they are attempted to be identified next.

There are three main trends that can be identified. First of all, with increasing frequency and keeping the other parameters constant, the value of β always drops. Physically this means that the slope of the temperature gradient along the wall becomes less steep with increasing frequency. This can be interpreted as; at the hot heat exchanger, the temperature becomes lower at specific points when increasing the frequency, and vice versa at the cold heat exchanger.

The second interesting trend is that the value of β increases with increasing temperature of the hot heat exchanger, whilst keeping the other parameters constant. This is true in all cases, except for the 100 mHz case with 144 mm strokelength. Here, the value at 70 °C is too high for this trend. However, since the difference at the latter case is really small, and all the other cases do present this behaviour, the trend is probably correct. The physical behaviour is exactly opposite of that described for the first trend, i.e. the temperature gradient gets steeper with increasing temperature of the hot heat exchanger.

The final trend that is identified is the decrease of β with increasing strokelength, as can be seen by investigating the difference between the two tables. This fact is true for every case, and actually has the largest effect of all three trends that are described here. The decrease in β with increasing strokelength might be explained by the fact that the temperature profile along the heat exchanger wall is more disturbed with increasing strokelength. Here, a disturbance means a change in temperature gradient along the heat exchanger wall when compared with a steady state case. The higher strokelength transports more heat downwards to the cold heat exchanger, and vice versa, and therefore lowers the temperature gradient along the wall.

Finally, as promised in the beginning of the section, a PV-diagram of one cycle of the experimental data will be given. This is mainly to show that more information can be gathered from the experimental set-up and the MATLAB function that has been written. The PV-diagram for the case of 25 mHz frequency, 72 mm strokelength and all three temperatures for the hot heat exchanger, is given in figure 20.

First of all, this figure shows that increasing the temperature of the hot heat exchanger significantly increases the gauge pressure inside the system. Next to that, one can clearly see that at the top position of the piston, which is at the smallest volume, the pressure increases due to the evaporation of the pentane. Similarly, at the cold heat exchanger the pressure drops due to the condensation of the pentane. Finally, one can clearly see from the PV-diagram that work can be produced using this experimental set-up, where the total amount of work is the area enclosed in the different PV-diagrams. It is also clear that for a higher temperature of the hot heat exchanger this area is much larger, and thus more work can be produced (as one would expect because more energy is put into the system as well).

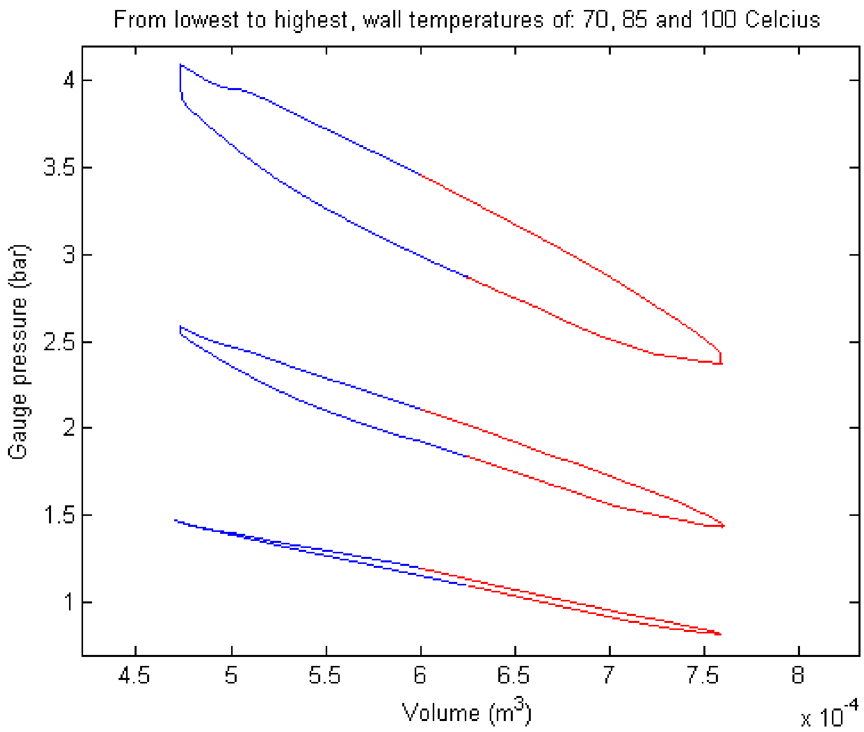

Figure 20: Plot of the PV-diagram for three experimental cases. For all plots the frequency was 25 mHz and the strokelength was 72 mm. From the lowest plot to the highest plot, the temperature of the hot heat exchanger increased from 70 °C up to 100 °C. The blue part of the section represents the first half of the cycle, and the red part the second half. All cycles are start at the equilibrium position, represented by the blue point with the lowest gauge pressure.

5 Conclusions

This chapter will provide the conclusions of the different aspects performed in this work. At first the conclusions about the validation of the LTP model and the DHX model will be given. Subsequently, the conclusions of the parametric study will be given. Then, the main conclusions of the experiments concerning the heat exchanger will be given. Finally, some limitations of this work will be stated, along with some suggestions for future work.

Model valdiation

In the model without a load two performance indicators were investigated, namely the operating frequency and the gradient along the heat exchanger. The main findings for the no-load models were as follows:

- The LTP model predicts the operating frequencies to be about one order of magnitude too high.
- The LTP model predicts the temperature gradients to be in the correct order of magnitude, albeit all values still seem to be too high in a physical sense.
- The DHX model predicts the operating frequencies quite well, although all predicted frequencies are too high.
- The DHX model predicts way too high power input gradients along the heat exchanger wall, and can thus not capture the correct behaviour for the no-load model.
- None of the trends spotted in the LTP model and the DHX model corresponded with the experimental results.

For the models with a load three performance indicators were investigated, namely the operating frequency, the gradient along the heat exchanger wall and the exergy efficiency. The main findings for the load models were as follows:

- Both the LTP model and the DHX model perform poorly for the 22 bar case, and these results differ significantly from the 5 bar and 9 bar cases. This can be explained by the fact that the experiments with 22 bar back-pressure were performed with an almost completely open valve, which thus approached a no-load case. This is confirmed by the resemblance of the 22 bar case with the no-load results.
- The LTP model performs poorly for all back-pressures and all performance indicators. It can thus be concluded that the LTP model is not suited to predict the behaviour of the ERPE with an included load.
- The DHX model predicts the frequency of the 5 bar and 9 bar case really well.
- The DHX model slightly overestimates the power input gradient along the heat exchanger wall, but the results for the 5 bar and 9 bar case are satisfactory.
- The DHX model overestimates the exergy efficiency by about one order of magnitude for the 5 bar and 9 bar case. As in the work on the NIFTE, it is expected that this can be improved by introducing thermal losses.

Overall it can be concluded that the DHX model performs much better than the LTP model for the cases with a load. For the cases without a load, the LTP model performs better; mainly because the predicted power input gradients of the DHX model are highly unrealistic. However, the final goal of this research is to develop a framework for an actual engine, which inherently has a load for power generation. Therefore, the results of the load cases should be viewed as more important, and therewith that the DHX model performs much better than the LTP model. The LTP model can't capture the behaviour of the experimental prototype. The DHX model, however, captures the behaviour well enough for this initial model, and can be used for future work on developing the ERPE.

Parametric study
The parametric study has been performed for the 5 bar and 9 bar case of the DHX model with a load. The main conclusion of the parametric study is that four electrical parameters were found to significantly change one or more of the performance indicators. The parameters C_{hx}, R_{th} and C_{vd} had a large influence on all three performance indicators, whilst C_{ld} only had a large influence on the power input gradient. The detailed influence of the four parameters on the performance indicators can be found in section 3.3, here the three most important observations are given:

- For values of C_{vd} which are more than two orders of magnitude lower than the nominal value, the exergy efficiency is predicted to rise above 90 % for the 5 bar case (see figure C7). For the 9 bar case the exergy efficiency rises up to around 30 %. Although these values are considered unrealistic, the trend in rising efficiency itself might be realistic, which is worth looking into. If correct, this means that increasing the average vapour volume or decreasing the heat capacity ratio of the working fluid can significantly increase the exergy efficiency.
- For an R_{th} between one and two orders of magnitude higher than the nominal value, there is a peak in exergy efficiency, as was clear from figure 12. This figure also shows that the exergy efficiency increases significantly more with increasing C_{hx}, at these values of R_{th}.
- Varying the hydrostatic capacitance C_{ld} only has a strong influence on the power input gradient. Therefore, a designer can alter the power input gradient to the desired value by varying C_{ld}, whilst keeping the other performance indicators at the same value.

The other electrical parameters yielded insignificant changes in the performance indicators, throughout a range of three orders of magnitude above and below their nominal values. The fact that varying these parameters did not have any significant influence, however, does not mean that the results are not interesting. The fact that the electrical parameters do not change the performance indicators, means that a designer can vary these parameters without influencing the performance indicators. This can, for example, result in a significantly easier design which requires lower production costs, whilst the performance of the engine is kept the same. Finally, it is stressed that one has to be careful with drawing conclusions, as has been done in this section. The parametric study is based on a linearised model, which itself has not proven to be in great correspondence with experimental results, and can therefore lead to wrong conclusions.

Experiments
Using the experimental set-up described in section 4.2, 18 experiments have been done. In these experiments, two different strokelengths, three different frequencies and three different temperatures for the hot heat exchanger were used. The main conclusion of these experiments is that the temperature profile of the heat exchanger can be modelled with a tanh function. This result is useful for future non-linear models, were the temperature profile has to be prescribed. This will be done by setting the temperature amplitude using the α parameter of the tanh function. The β parameter, which describes the gradient of the tanh function, has been identified from the different experiments with normalized results. This showed that the value for β only deviated slightly between the different cases, and therefore the same value of β can be used

in a sufficient range of operating conditions. The suggested value for β is 2.56, which is the average of all the experimental results. It should be kept in mind that this is the gradient for the normalized results, were the length dimension runs from -0.5 to +0.5 and the temperature runs from -1 to +1 (thus $\alpha = 1$). For a non-normalized case, the value for the gradient is the product of α and β, which should be properly scaled when changing the length axis.

Finally, if for future work one wants to model the change of β for changing operating conditions, one has to at least model the following identified trends:

- The value for β increases with increasing temperature of the hot heat exchanger.
- The value for β decreases with increasing operating frequency.
- The value for β decreases with increasing strokelength of the piston.

Limitations of the study and future work

The first and most important limitation of the presented work is obviously the linearisation of the governing equations. In the previous work done on the NIFTE, it was found that quite accurate predictions could be made from an analogous linear model. However, in the current work this predictive power has declined, which is mainly thought to be caused by the non-linear components of the ERPE. Examples of the non-linear components are the heat exchanger, the piston valve (as shown in figure 2) and the check valve system at the load. For future work on the ERPE, it is therefore interesting to use a non-linear model, as was eventually also done for the NIFTE [18]. Next to an expected increase in predictive power, this model will be able to predict actual pressure amplitudes. This is a great improvement from the linear models presented in this report, were only ratio's of amplitudes could be predicted. This will provide a new, and physically very important performance indicator, which can also be tested against experimental data.

Another main point that has to be improved is the quality and quantity of the experimental data. For the current work there were six data sets available, of which only three for the case with a load. In these three cases, not only the back-pressure was changed, but also the valve setting. It is therefore really hard to pinpoint certain behaviour to a specific change. Due to the latter, and the absence of a lot of experimental data, it is really hard to validate the model. For future validation purposes, there definitely has to be more experimental data available, in which also the gradients along the heat exchanger have to be measured for every case. Finally, the sampling rate of the data should be significantly higher, especially for the no-load cases.

When in the future a non-linear model is produced and validated by experimental results, the non-linear model can be used to optimize the design of the ERPE prototype. This could be optimized for e.g. efficiency, power output etc., or combinations hereof. This should eventually lead to full-scale ERPE designs which can be used for actual power generation using low-grade heat.

The main problem in the experiments to determine the temperature gradient along the heat exchanger, was found to be the cooling at the cold heat exchanger. The silicon tubing did not have enough cooling power. Eventually a steady state could always be reached, but at this steady state the temperature of the wall at the cold heat exchanger was still a lot higher than the temperature of the cooling water (around 20 °C higher for the 100 °C hot heat exchanger case). Therefore, for future experiments, the cold heat exchanger has to be improved, e.g. by using copper tubing instead of silicon tubing.

Finally, for future work, it would be interesting to look at the other results from the experimental set-up. This includes PV-diagrams, the temperature at the wall were the piston is (thus the temperature the fluid is experiencing), the temperature amplitude at one point of the wall during one cycle etc. This could lead to some very interesting insights into the heat exchanger and thermodynamic processes in these oscillating flow engines.

References

[1] S. Shafiee, E. Topal, When will fossil fuel reserves be diminished?, Energy Policy 37 (1) (2009) 181–189.

[2] Y. Ammar, S. Joyce, R. Norman, Y. Wang, A. P. Roskilly, Low grade thermal energy sources and uses from the process industry in the UK, Applied Energy 89 (1) (2012) 3–20.

[3] C. Chan, J. Ling-Chin, A. Roskilly, Reprint of: A review of chemical heat pumps, thermodynamic cycles and thermal energy storage technologies for low grade heat utilisation, Applied Thermal Engineering 53 (2) (2013) 160–176.

[4] T. Smith, Thermally Driven Oscillations in Dynamic Applications, Ph.D. thesis, University of Cambridge (2006).

[5] C. Stammers, The operation of the Fluidyne heat engine at low differential temperatures, Journal of Sound and Vibration 63 (4) (1979) 507–516.

[6] G. W. Swift, Thermoacoustic engines, The Journal of the Acoustical Society of America 84 (4) (1988) 1145.

[7] J. Wheatley, An intrinsically irreversible thermoacoustic heat engine, The Journal of the Acoustical Society of America 74 (1) (1983) 153.

[8] S. Carnot, Réflexions sur la puissance motrice du feu et sur les machines propres à développer cette puissanceÂă(Google eBook), Gauthier-Villars, 1824.

[9] G. W. Swift, Thermoacoustics: A Unifying Perspective for Some Engines and Refrigerators, 2002.

[10] T. Smith, Power Dense Thermofluidic Oscillators for High Load Applications, in: 2nd International Energy Conversion Engineering Conference, International Energy Conversion Engineering Conference (IECEC), American Institute of Aeronautics and Astronautics, 2004.

[11] T. Smith, Asymmetric heat transfer in vapour cycle liquid-piston engines, in: 12th International Stirling Engine Conference and Technology Exhibition, Durham, 2005, pp. 302–314.

[12] A. Samoilov, V. Kirillov, N. Kuzin, A. Kronberg, M. Gloushenkov, A. Taleb, C. Markides, An External Combustion Heat Engine with Phase-Change Working fluid, in: 13th UK Heat Transfer Conference, London, 2013, pp. 93–1.

[13] C. N. Markides, T. C. Smith, A dynamic model for the efficiency optimization of an oscillatory low grade heat engine, Energy 36 (12) (2011) 6967–6980.

[14] R. Solanki, A. Galindo, C. N. Markides, Dynamic modelling of a two-phase thermofluidic oscillator for efficient low grade heat utilization: Effect of fluid inertia, Applied Energy 89 (1) (2012) 156–163.

[15] R. Solanki, A. Galindo, C. N. Markides, The role of heat exchange on the behaviour of an oscillatory two-phase low-grade heat engine, Applied Thermal Engineering 53 (2) (2013) 177–187.

[16] R. Solanki, R. Mathie, A. Galindo, C. N. Markides, Modelling of a two-phase thermofluidic oscillator for low-grade heat utilisation: Accounting for irreversible thermal losses, Applied Energy 106 (2013) 337–354.

[17] B. Huang, M. Chuang, System design of orifice pulse-tube refrigerator using linear flow network analysis, Cryogenics 36 (11) (1996) 889–902.

[18] C. Markides, A. Osuolale, R. Solanki, G. Stan, Nonlinear heat transfer processes in a two-phase thermofluidic oscillator, Applied Energy 104 (2013) 958–977.

A Nominal values for validation

The values in this appendix are derived from the design of the experimental set-up in Novisibirsk, Russia. Next to that, the changing working fluid properties with changing back-pressure are acquired from the NIST database[1].

Table A1: Nominal values for the variables that do not depend on the back-pressure and are assumed to be constant.

Variable	Nominal Value	Units	Variable	Nominal Value	Units
$l_{\text{dc (without piston)}}$	0.077	m	$\overline{D_{\text{p}}}$	0.017	m
l_{wc}	0.240	m	$V_{0,\text{dc}}$	1.75×10^{-5}	m^3
l_{ct}	0.600	m	$d_{channel}$	0.002	m
l_{sb}	0.058	m	$V_{0,\text{wc}}$	1.79×10^{-5}	m^3
D_{dc}	0.027	m	h	10,000	$W\ m^{-2}\ K^{-1}$
D_{wc}	0.030	m	mp	0.42	kg
D_{ct}	0.004	m	k	1500	$N\ m^{-1}$
h_{p}	0.390	m	$\rho_{\text{stainless steel}}$	7800	$kg\ m^{-3}$
$c_{p,stainless\ steel}$	500	$J\ kg^{-1}\ K^{-1}$			

Table A2: Nominal values for the electrical parameters (R,L,C) at different back-pressures

Electrical Parameters' Nominal Value at different back pressures							
Parameter	**3.58 bar**	**5 bar**	**5.5 bar**	**8.22 bar**	**9 bar**	**22 bar**	**Units**
A_s	6.94×10^{-5}	7.18×10^{-5}	7.26×10^{-5}	7.61×10^{-5}	7.70×10^{-5}	8.85×10^{-5}	m^2
$R_{l,1}$	1.86×10^{7}	1.86×10^{7}	1.86×10^{7}	1.86×10^{7}	1.86×10^{7}	1.86×10^{7}	$kg\ m^{-4}\ s^{-1}$
$R_{l,2}$	1.02×10^{6}	1.02×10^{6}	1.02×10^{6}	1.02×10^{6}	1.02×10^{6}	1.02×10^{6}	$kg\ m^{-4}\ s^{-1}$
R_p	1.76×10^{5}	1.76×10^{5}	1.76×10^{5}	1.76×10^{5}	1.76×10^{5}	1.76×10^{5}	$kg\ m^{-4}\ s^{-1}$
$R_{sb,l}$	1.68×10^{8}	1.68×10^{8}	1.68×10^{8}	1.68×10^{8}	1.68×10^{8}	1.68×10^{8}	$kg\ m^{-4}\ s^{-1}$
$R_{sb,p}$	1.22×10^{6}	1.22×10^{6}	1.22×10^{6}	1.22×10^{6}	1.22×10^{6}	1.22×10^{6}	$kg\ m^{-4}\ s^{-1}$
$R_{l,dc}$	4.613×10^{3}	4.612×10^{3}	4.612×10^{3}	4.612×10^{3}	4.612×10^{3}	4.61×10^{3}	$kg\ m^{-4}\ s^{-1}$
R_{ct}	1.08×10^{8}	1.08×10^{8}	1.08×10^{8}	1.08×10^{8}	1.08×10^{8}	1.08×10^{8}	$kg\ m^{-4}\ s^{-1}$
R_{th}	6.11×10^{10}	1.04×10^{11}	1.21×10^{11}	2.26×10^{11}	2.60×10^{11}	9.92×10^{11}	$kg\ m^{-4}\ s^{-1}$
$R_{l,wc}{}^{+}$	6.08×10^{3}	6.08×10^{3}	6.08×10^{3}	6.08×10^{3}	6.08×10^{3}	6.08×10^{3}	$kg\ m^{-4}\ s^{-1}$
L_l	4.48×10^{7}	4.48×10^{7}	4.48×10^{7}	4.48×10^{7}	4.48×10^{7}	4.48×10^{7}	$kg\ m^{-4}$
L_p	7.76×10^{6}	7.76×10^{6}	7.76×10^{6}	7.76×10^{6}	7.76×10^{6}	7.76×10^{6}	$kg\ m^{-4}$
$L_{sb,l}$	1.84×10^{7}	1.84×10^{7}	1.84×10^{7}	1.84×10^{7}	1.84×10^{7}	1.84×10^{7}	$kg\ m^{-4}$
$L_{sb,p}$	3.01×10^{6}	3.01×10^{6}	3.01×10^{6}	3.01×10^{6}	3.01×10^{6}	3.01×10^{6}	$kg\ m^{-4}$
$L_{l,dc}$	7.43×10^{5}	7.44×10^{5}	7.44×10^{5}	7.45×10^{5}	7.45×10^{5}	7.45×10^{5}	$kg\ m^{-4}$
L_{ct}	4.77×10^{7}	4.77×10^{7}	4.77×10^{7}	4.77×10^{7}	4.77×10^{7}	4.77×10^{7}	$kg\ m^{-4}$
$L_{l,wc}{}^{+}$	3.35×10^{5}	3.35×10^{5}	3.35×10^{5}	3.35×10^{5}	3.35×10^{5}	3.35×10^{5}	$kg\ m^{-4}$
C_l	1.32×10^{-7}	1.32×10^{-7}	1.32×10^{-7}	1.32×10^{-7}	1.32×10^{-7}	1.32×10^{-7}	$m^4\ s^2\ kg^{-1}$
C_p	3.62×10^{-11}	3.62×10^{-11}	3.62×10^{-11}	3.62×10^{-11}	3.62×10^{-11}	3.62×10^{-11}	$m^4\ s^2\ kg^{-1}$
$C_{l,dc}$	5.99×10^{-8}	5.99×10^{-8}	5.99×10^{-8}	5.99×10^{-8}	5.99×10^{-8}	5.99×10^{-8}	$m^4\ s^2\ kg^{-1}$
$C_{v,dc}$	3.59×10^{-11}	$2.55\times10\text{-}^{11}$	2.31×10^{-11}	1.53×10^{-11}	$1.\ 39\times10^{-11}$	5.32×10^{-12}	$m^4\ s^2\ kg^{-1}$
$C_{l,wc}{}^{+}$	7.31×10^{-8}	7.31×10^{-8}	7.31×10^{-8}	7.31×10^{-8}	7.31×10^{-8}	7.31×10^{-8}	$m^4\ s^2\ kg^{-1}$
$C_{v,wc}{}^{+}$	2.98×10^{-11}	2.13×10^{-11}	1.93×10^{-11}	1.29×10^{-11}	1.17×10^{-11}	4.7×10^{-12}	$m^4\ s^2\ kg^{-1}$
C_{hx}*	2.18×10^{-11}	1.28×10^{-11}	1.10×10^{-11}	5.89×10^{-12}	5.12×10^{-12}	1.34×10^{-12}	$m^4\ s^2\ kg^{-1}$

$^{+}$Only appear in the **no load** model; *DHX only

[1] http://webbook.nist.gov/chemistry/fluid/

B Load models

This appendix presents the fitting of the load models, according to experimental measurements, for the two cases which weren't presented in the main report.

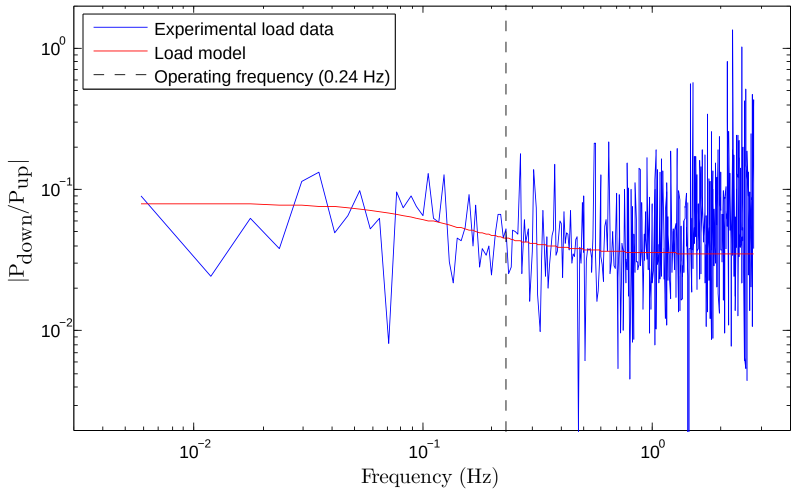

Figure B1: In blue: plot of the amplitude ratio $|P_{down}/P_{up}|$ of the experimental data with the valve set to the intermediate steady flow resistance and 9 bar back-pressure. In Red: plot of the fitted load model according to equation 2.30. In Black: a dotted line which shows the frequency at which the ERPE prototype was oscillating with the according valve setting and back-pressure.

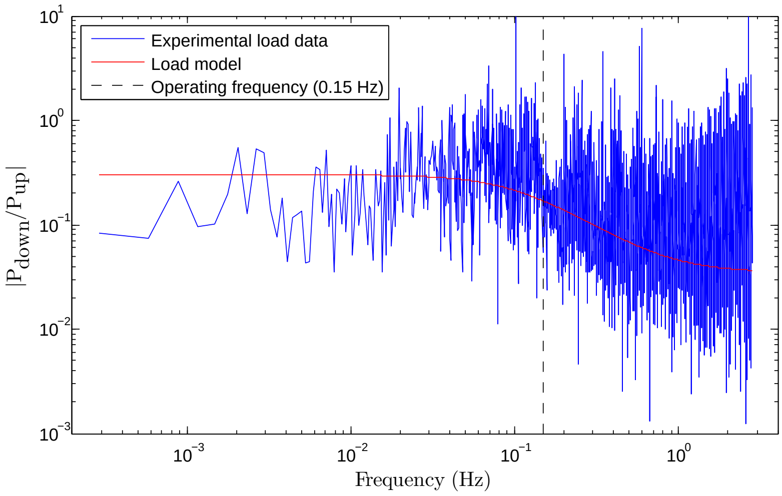

Figure B2: In blue: plot of the amplitude ratio $|P_{down}/P_{up}|$ of the experimental data with the valve set to the lowest steady flow resistance and 22 bar back-pressure. In Red: plot of the fitted load model according to equation 2.30. In Black: a dotted line which shows the frequency at which the ERPE prototype was oscillating with the according valve setting and back-pressure.

C Figures of the parametric study

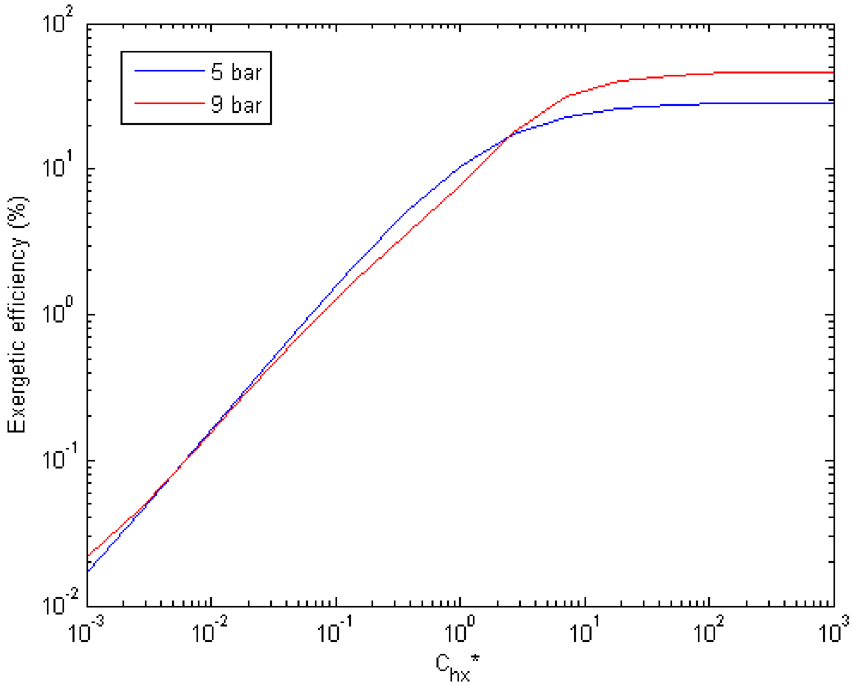

Figure C1: Parametric study: Exergy efficiency as function of C_{hx}, where C_{hx}^* is the normalized value for C_{hx}. Note that the nominal value of C_{hx} is different for the 5 bar case (blue) and the 9 bar case (red).

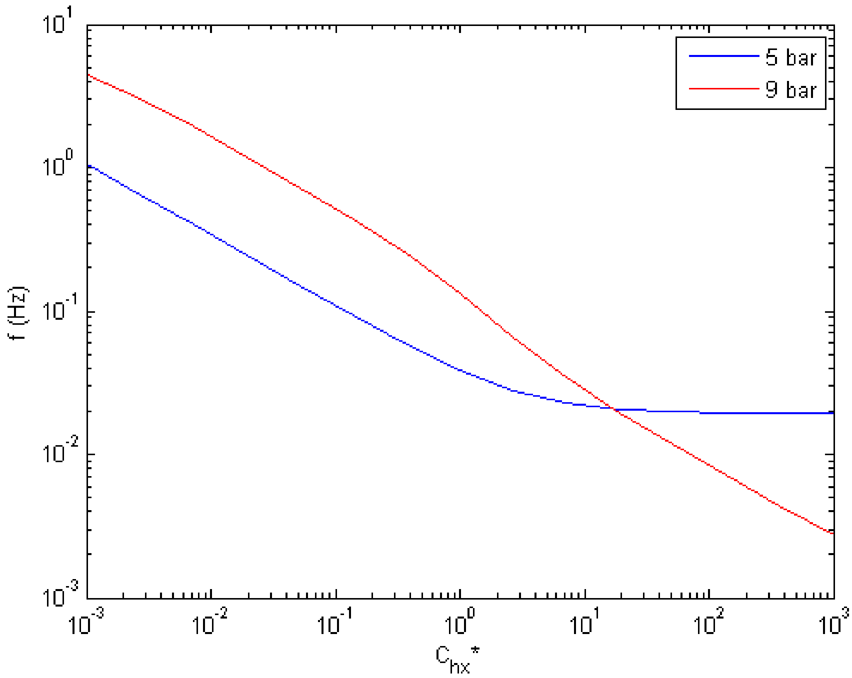

Figure C2: Parametric study: Frequency as function of C_{hx}, where C_{hx}^* is the normalized value for C_{hx}. Note that the nominal value of C_{hx} is different for the 5 bar case (blue) and the 9 bar case (red).

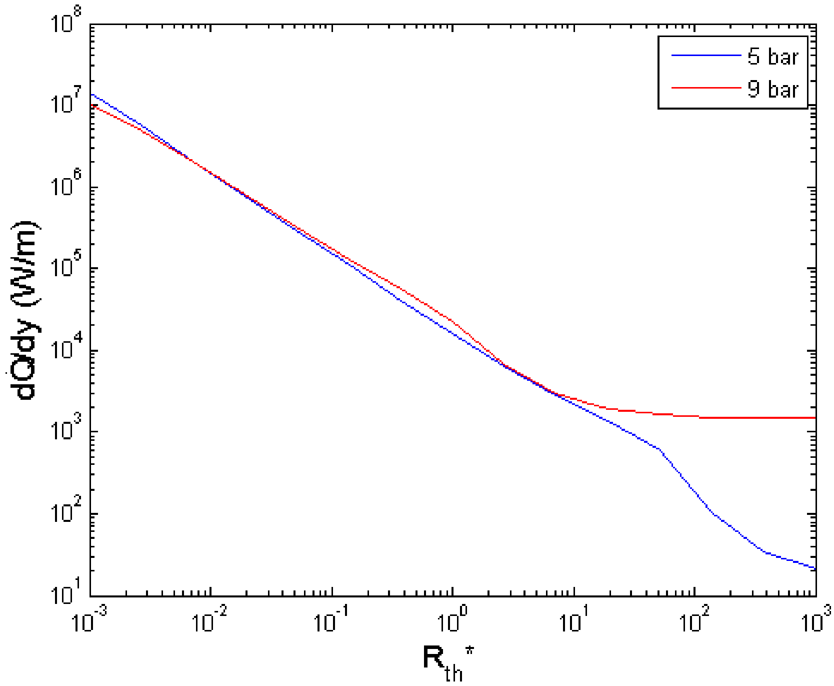

Figure C3: Parametric study: Power input gradient as function of R_{th}, where R_{th}^* is the normalized value for R_{th}. Note that the nominal value of R_{th} is different for the 5 bar case (blue) and the 9 bar case (red).

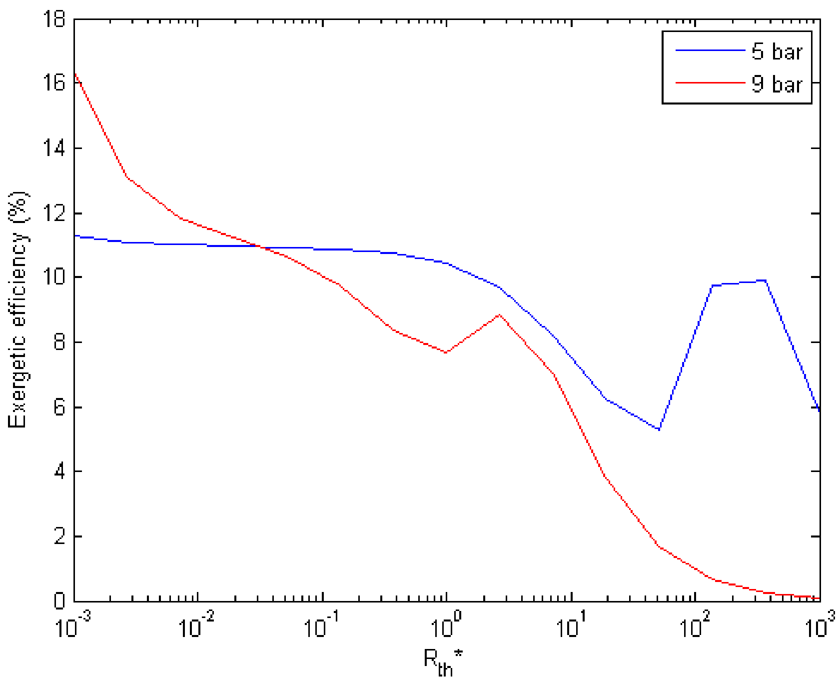

Figure C4: Parametric study: Exergy efficiency as function of R_{th}, where R_{th}^* is the normalized value for R_{th}. Note that the nominal value of R_{th} is different for the 5 bar case (blue) and the 9 bar case (red).

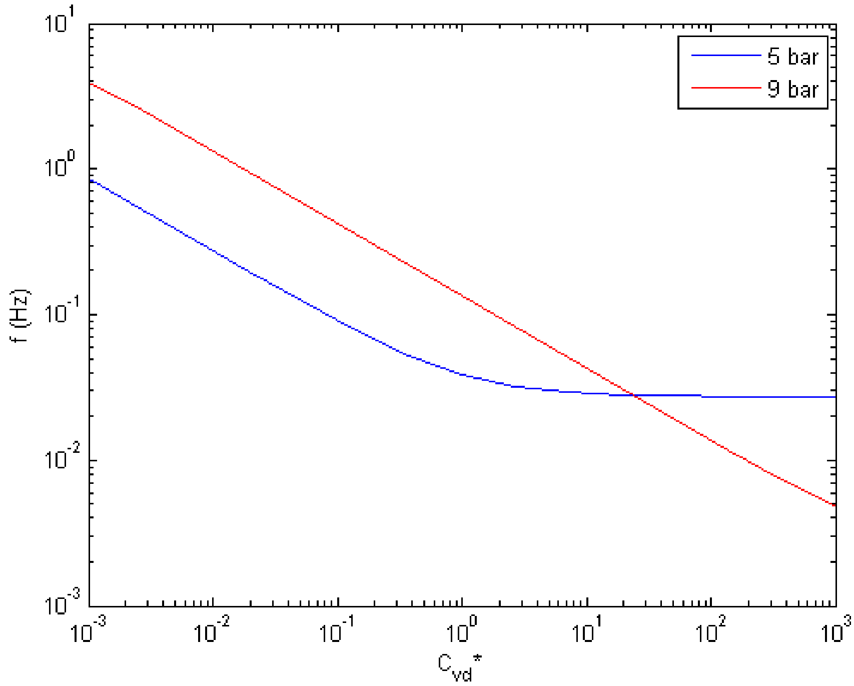

Figure C5: Parametric study: Frequency as function of C_{vd}, where C^*_{vd} is the normalized value for C_{vd}. Note that the nominal value of C_{vd} is different for the 5 bar case (blue) and the 9 bar case (red).

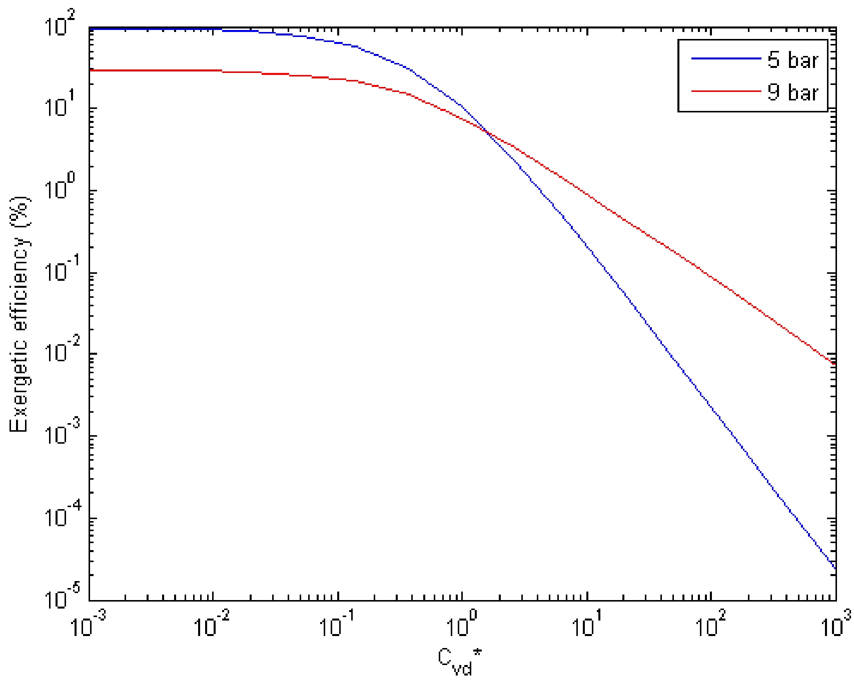

Figure C6: Parametric study: Efficiency as function of C_{vd}, where C^*_{vd} is the normalized value for C_{vd}. Note that the nominal value of C_{vd} is different for the 5 bar case (blue) and the 9 bar case (red).

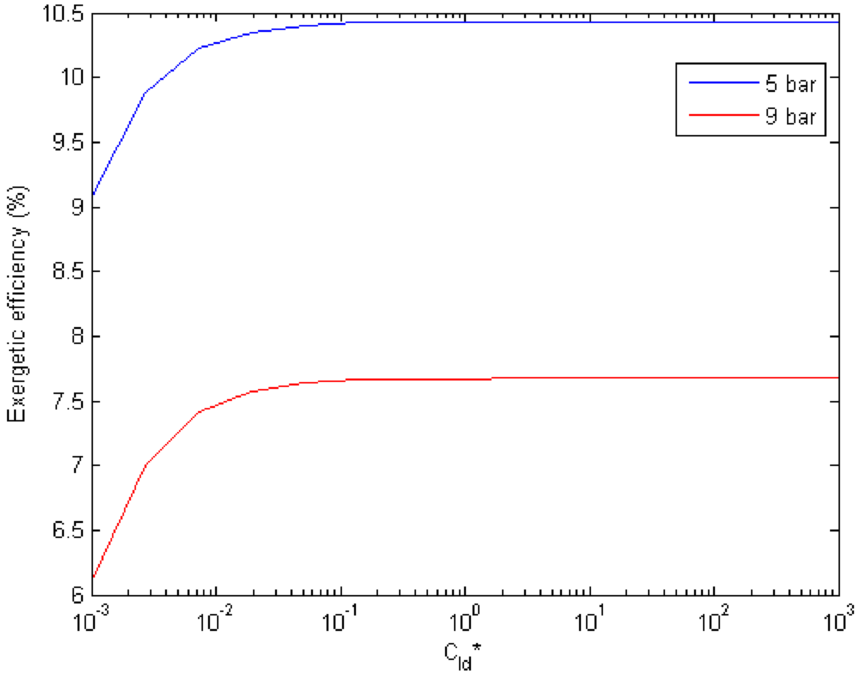

Figure C7: Parametric study: Efficiency as function of C_{ld}, where C^*_{ld} is the normalized value for C_{ld}. Note that the nominal value of C_{ld} is different for the 5 bar case (blue) and the 9 bar case (red).